Journal of *Marine Science and Engineering*

MDPI

Article

Two Processes of Anglesite Formation and a Model of Secondary Supergene Enrichment of Bi and Ag in Seafloor Hydrothermal Sulfide Deposits

Zhigang Zeng [1,2,3,*], Zuxing Chen [1,4] and Haiyan Qi [1,4]

[1] Seafloor Hydrothermal Activity Laboratory, CAS Key Laboratory of Marine Geology and Environment, Institute of Oceanology, Chinese Academy of Sciences, Qingdao 266071, China; chenzuxing@qdio.ac.cn (Z.C.); qihaiyan@qdio.ac.cn (H.Q.)
[2] Laboratory for Marine Mineral Resources, Qingdao National Laboratory for Marine Science and Technology, Qingdao 266071, China
[3] College of Marine Sciences, University of Chinese Academy of Sciences, Beijing 100049, China
[4] Center for Ocean Mega-Science, Chinese Academy of Sciences, 7 Nanhai Road, Qingdao 266071, China
* Correspondence: zgzeng@qdio.ac.cn; Tel.: +86-532-8289-8525

Abstract: The in situ element concentrations and the sulfur (S), and lead (Pb) isotopic compositions in anglesite were investigated for samples from seafloor hydrothermal fields in the Okinawa Trough (OT), Western Pacific. The anglesite grains are of two kinds: (1) low Pb/high S primary hydrothermal anglesite (PHA), which is formed by mixing of fluid and seawater, and (2) high Pb/low S secondary supergene anglesite (SSA), which is the product of low-temperature (<100 °C) alteration of galena in the seawater environment. The Ag and Bi in the SSA go through a second enrichment process during the formation of high Pb/low S anglesite by galena alteration, indicating that the SSA and galena, which may be the major minerals host for considerable quantities of Ag and Bi, are potentially Ag-Bi-enriched in the back-arc hydrothermal field. Moreover, REEs, S and Pb in the OT anglesite are likely to have been leached by fluids from local sub-seafloor volcanic rocks and/or sediments. A knowledge of the anglesite is useful for understanding the influence of volcanic rocks, sediments and altered subducted oceanic plate in hydrothermal systems, showing how trace metals behave during the formation of secondary minerals.

Keywords: anglesite; element distribution and mobility; supergene Ag–Bi enrichment; sulfide; hydrothermal vent

Citation: Zeng, Z.; Chen, Z.; Qi, H. Two Processes of Anglesite Formation and a Model of Secondary Supergene Enrichment of Bi and Ag in Seafloor Hydrothermal Sulfide Deposits. *J. Mar. Sci. Eng.* **2022**, *10*, 35. https://doi.org/10.3390/jmse10010035

Academic Editor: János Kovács

Received: 17 November 2021
Accepted: 19 December 2021
Published: 31 December 2021

1. Introduction

Anglesite ($PbSO_4$) has been widely identified as a supergene weathering product of primary galena in oxidation zones in supergene weathering deposits and mine-waste sites [1–15]. Oxidation and acid-neutralization reactions partially dissociate the galena and promote the development of secondary supergene anglesite [16], which then surrounds and directly replaces galena contained within the anglesite [17], and the galena in situ appears to be directly oxidized and partly or totally replaced by anglesite along its cleavage planes and grain boundaries [11,18]. For example, in the Sidi Flah mine, Morocco, galena is locally surrounded by a halo of altered anglesite $PbSO_4$ [19]. Replacement also takes place at the rim of galena grains as well as along the typical cleavage planes [7], which is dissolved releasing Pb^{2+} and SO_4^{2-} ions at high pH (>9) oxidizing environment [20], and the solution interacting with the galena surface is strongly undersaturated with respect to both the primary galena and secondary supergene anglesite ($PbSO_4$) [21]. Supergene weathering of primary galena leads to the formation of thermodynamically more stable secondary anglesite. Whether or not the anglesite is stable depends on its pH, sulfur and lead activity, partial pressure of CO_2 (P_{CO2}) and temperature in the seawater [7,11]. Under

oxidizing conditions, anglesite is stable between pH values of about 0.4 and 5.0 [22], and the reported value of the solubility constant for anglesite (K_{sp} = 10–7.79) indicates that it is relatively insoluble [23].

However, replacement of galena by anglesite does not produce acid [24]. Locally occurring iron sulfides undergoing oxidation acidify solutions and provide ferric ions, which are important oxidizing agents [10], and anglesite preferentially forms in such microenvironments [3]. In the first phase of this process, oxidation takes place along cleavage planes and grain boundaries, and galena weathers to anglesite [25]. Moreover, in the supergene Cu-Pb-Zn-V ores of the Oriental High Atlas, Morocco, anglesite is observed in fractures and cleavage planes in galena, and as a thin rim around it [26]. It is also found throughout the waste dumps at Callahan Cu-Zn-Pb mine in the Goose Pond tidal estuary, Maine, USA, as rims on masses of galena, and inside thin fractures that cut across grains of galena and surrounding minerals and in veinlets and fracture sets that redistribute Pb [6].

However, anglesite precipitation can effectively control the attenuation process of fluid Pb concentration [27]. Weathering reactions control the release and transport of Pb and other metals in acidic and near-neutral conditions in surface environments [6,28]. In the Butte mining district, Montana, the low Pb levels may be partly explained by the low solubility of anglesite, especially in more sulfate-rich waters, or by the low solubility of galena in the sulfidic waters of the flooded West Camp mining district in Butte [29].

Anglesite also acts an important solid-phase control on the aqueous mobility of Pb in the Santa Lucia mine, Cuba [16]. The main mechanism controlling the mobility of As, Ba and Pb is the precipitation of secondary supergene anglesite [16]. Geochemical modeling indicates that leaching solutions are supersaturated with anglesite over the entire pH range, showing that anglesite controls the As and Pb, and to a lesser degree the Zn and Cu, unless the pH drops below 3.0 [27]. Furthermore, electron microprobe analyses (EMPA) of anglesite in the waste rocks of the abandoned Seobo tungsten mine in Korea have shown notable Cu concentrations up to 4.6 wt.% [27].

Although the mineral characteristics and chemical compositions of anglesite provide important information about weathering reactions as well as fluid/solid interaction and supergene processes, little is known about the chemical composition of anglesites from seafloor hydrothermal systems, since it occurs only as a minor mineral in sulfide samples, and also due to its secondary supergene genesis in sulfide deposits. The study of element concentrations and isotopic compositions in anglesite from seafloor hydrothermal systems is an important means of understanding element enrichment during supergene oxidation of hydrothermal sulfide deposits, allowing both metal sources and reconstruction of the physicochemical conditions of their preservation to be inferred. In this study, in situ major, trace element abundance, sulfur and lead isotopic compositions in anglesite were measured for the first time in seafloor hydrothermal fields from the back-arc Okinawa Trough (OT) (Figure 1). The isotopic compositions of S and Pb in the anglesite and the abundance of in situ elements from seafloor sulfide deposits are described in combination with the chemical compositions of associated galena and other sulfide minerals. The hydrothermal and seawater contributions of sulfur and are described in an attempt to reveal the mechanisms of element enrichment and the isotope variations in the anglesite, as well as the anglesite formation processes in seafloor hydrothermal systems generally for understanding seafloor massive sulfide deposit preservation and supergene oxidation processes.

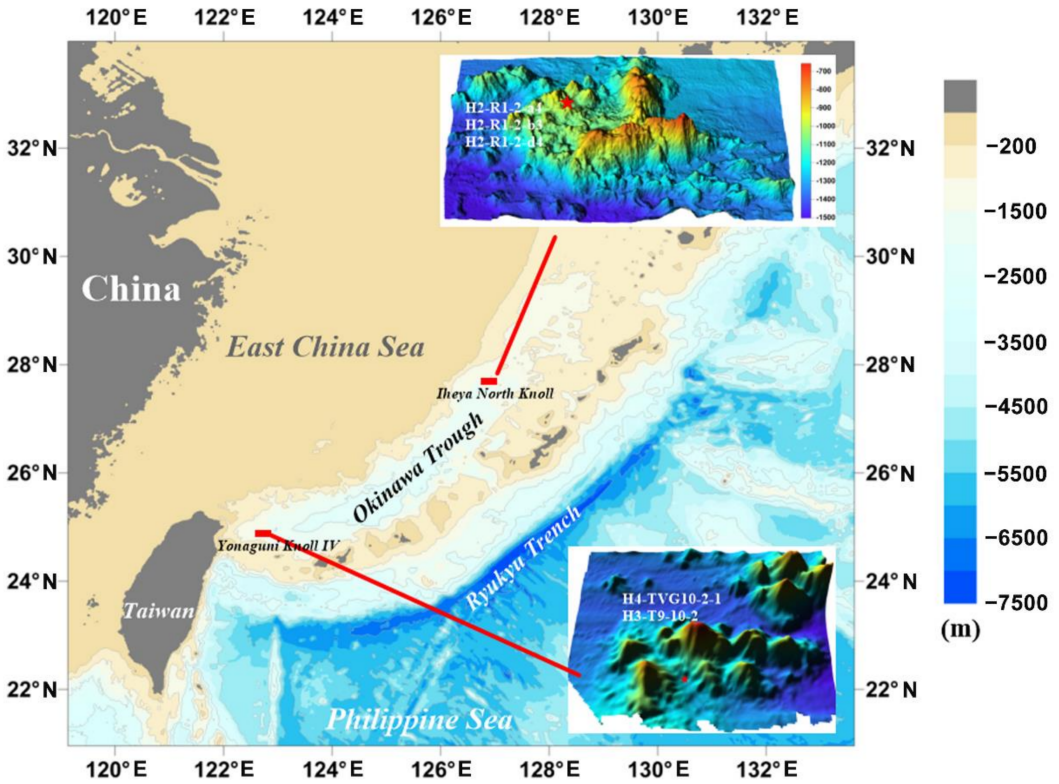

Figure 1. Locations of seafloor hydrothermal sulfide and sulfate samples from the Yonaguni Knoll IV, Irabu Knoll and Iheya North Knoll hydrothermal fields in the Okinawa Trough (red rectangle = location of seafloor hydrothermal field; red star = sulfide and sulfate sampling site).

2. Geological Setting

The OT is at the rifting-to-spreading stage of a back-arc basin, exhibiting the development of normal faulting of brittle crustal rocks and frequent magma intrusions. The OT topography changes markedly from the central to southern parts of the trough, with deepening of the trough floor and steepening of the continental slope, accompanied by en echelon intra-trough grabens [30,31]. The tectonic and geophysical properties of the OT also differ from north to south, with crustal thickness decreasing southwards. The southern part shows variable gravity and linear magnetic anomalies, with greatest heat flow in the central part. Most of the crust in the OT is transitional, although oceanic crust probably appears in some grabens in both the central and southern parts [32]. It provides a favorable geological environment for the development of seafloor hydrothermal systems [31–34].

As of 2015, the InterRidge Vents Database had recorded at least 15 deep-sea hydrothermal fields in the OT, including the Minami-Ensei [35]; Iheya North [36–38]; Jade [39,40]; Hakurei [41]; Irabu Knoll [42,43]; Hatoma [44,45]; Yonaguni Knoll IV [46–48] and Tangyin [34,49] hydrothermal fields. This study focuses on the Iheya North Knoll and Yonaguni Knoll IV hydrothermal fields.

The Iheya North Knoll hydrothermal field (27°47.2′ N, 126°53.9′ E) is located in about 1000 m water depth along the eastern slope of a small knoll, which is part of the Iheya North Knoll volcanic complex [31] (Figure 1). Seismic studies around the Iheya North Knoll have indicated relatively disordered seismic reflectors as deep as 400–500 mbsf (meters below seafloor) in the central valley, surrounded by small knolls [50], indicating the presence of pumiceous volcaniclastic flow deposits beneath hemipelagic surficial sediments, rather than massive igneous rocks [31]. About 10 active hydrothermal mounds, aligned north to south, are concentrated in a small region [31], many of which host active fluid vents and sulfide and sulfate mineralization [31]. A large mound (named North Big Chimney) more than 30 m high is associated with vigorous venting of clear fluid and with the highest

temperature of 311 °C, and appears to mark the center of hydrothermal activity [36]. The vent fluids have lower alkalinity (0.5–3.6 mmol l–1), NH^{4+} (1.9–2.6 mmol kg^{-1}) and Cl- (441–458 mmol kg^{-1}), indicating phase separation of the fluid beneath the seafloor [37]. Mineralization in the Iheya North Knoll included sulfide and sulfate mineralization [31]. For instance, the main sulfate minerals are barite, gypsum and anhydrite. Sulfide consists mainly of sphalerite, galena, pyrite, chalcopyrite, marcasite, wurtzite and tennantite–tetrahedrite. Luzonite, freieslebenite and covellite are also present in small amounts [31]. However, it is possible to use hydrothermal sulfide and its inclusions to trace the deep circulation processes of fluid in the future.

The Yonaguni Knoll IV hydrothermal field is situated in an elongated valley [48] (Figure 1). The valley is mostly covered with muddy sediment, except for the active vent field and volcanic rocks on its northern slope. Suzuki et al. [48] distinguished five types of mineralization: (1) anhydrite-rich chimneys; (2) massive Zn–Pb–Cu sulfides; (3) Ba–As chimneys; (4) Mn-rich chimneys and (5) a pavement of silicified sediment. In addition, diverse styles of fluid venting were found to occur within the hydrothermal field, including slightly Cl-enriched (614–635 mmol kg^{-1}) and depleted (376–491 mmol kg^{-1}) fluids associated with the discharge of liquid droplets of CO_2 [48]. However, there is a relationship between the tectonic setting, magmatism, mineralization, fluid–rock interaction and sedimentary processes in the seafloor hydrothermal system (e.g., Iheya North Knoll and Yonaguni Knoll IV) and the response, adaptation, record and action of organism, and it will be interesting to explore the synergetic metallogenic mechanism of magma, fluid, rock, sediment, seawater and organisms in the seafloor hydrothermal field in the future.

3. Sampling and Methods

3.1. Specimen and Analytical Techniques

Anglesite, galena and other sulfide mineral samples from seafloor hydrothermal sulfide deposits were collected in 2014 and 2016 during the HOBAB 2, 3 and 4 cruises of hydrothermal fields in the OT. Samples were taken from the Iheya North (samples H2-R1-2-a4, -b3, -d4), and the Yonaguni Knoll IV (samples H4-TVG10-2-1, and H3-T9-10-2) hydrothermal fields (Figures 1 and 2).

Figure 2. Photographs of hand specimens.

The anglesite, associated galena and other sulfide mineral samples from selected seafloor sulfide and sulfate deposits were analyzed using thin sections to determine the content of major and trace elements and S and Pb isotopic compositions. Reflected and transmitted light microscopy techniques were used to reveal the external morphology and internal structure of samples. Anglesite, associated galena and other sulfide minerals and microstructures were determined using back-scattered electron (BSE) images and an Oxford Instruments INCA X-Max energy dispersive spectrometer (EDS) on a TESCAN VEGA 3 LMH scanning electron microscope (SEM) at the Institute of Oceanology, Chinese Academy of Sciences.

3.2. In Situ Major Element Determination

The major element compositions of the anglesite, associated galena, pyrite, sphalerite and chalcopyrite were determined using a JXA-8230 electron microprobe analyzer (EMPA) at the State Key Laboratory of Continental Dynamics, Northwest University, Xian, China. The instrument was operated at a 15 kV acceleration voltage, 10 nA beam current and 2 μm beam diameter. The following reference materials were used for wavelength dispersive spectrometry measurements and calibrations: pyrite (for S and Fe); chalcopyrite (for Cu); sphalerite (for Zn); galena (for Pb) and skutterudite (for As). Pure metals were Au, Ag, Cd, Sb, Se, Ni, Co and Cr, and the silicates were diopside (for Ca, Mg and Si); albite (for Al); bustamite (for Mn); rutile (for Ti); apatite (for Sr) and barite (for Ba). The test accuracy for major elements in the sulfides and sulfates was better than 5%. The detection limits for selected trace elements were approximately within the range of 0.01 to 0.12 wt.% (Table S1).

3.3. In Situ Trace Element Determination

In situ measurements of trace elements in the anglesite, associated galena, pyrite, sphalerite and chalcopyrite were determined using a laser-ablation inductively coupled plasma mass spectrometer (LA-ICP-MS) at the State Key Laboratory of Biogeology and Environmental Geology, China University of Geosciences, Wuhan. A GeoLas Pro 193 nm ArF excimer laser was applied to analyze the samples. Laser energy was 80 mJ, and frequency was 6 Hz with a 44 μm diameter ablation spot. Acquisition of ion-signal intensity was performed using an Agilent 7500x ICP-MS instrument. Helium was used as the carrier gas, which was mixed with argon via a T-connector before entering the ICP-MS. Each measurement incorporated a background acquisition of approximately 30 s (gas blank) followed by 50 s of data acquisition from the sample, using ICPMSDataCal software to quantitatively calibrate trace element contents [51,52]. Fe, Cu, Zn and Pb were selected as the internal standards for data reduction. NIST 610 glass was used as the external standard, which was analyzed every 10 spots to monitor for any instrument drifts. The accuracy was determined with respect to the NIST 610 reference glass and was assessed to be better than 10% (1σ).

The rare earth element (REE) contents were normalized to Cl-chondrites (subscript $_{CN}$) [53]. The Eu and Ce anomalies were assessed as $(Eu/Eu^*)_{CN} = Eu_{CN}/(Sm_{CN} + Gd_{CN})^{0.5}$ and $(Ce/Ce^*)_{CN} = Ce_{CN}/(La_{CN} + Pr_{CN})^{0.5}$.

3.4. In Situ S Isotope Analysis

In situ measurements of S isotope ratios of the anglesite and associated galena, pyrite, sphalerite and chalcopyrite were conducted on double-sided-polished slices (DSPSs) of these minerals using a 193 nm femtosecond laser-ablation multi-collector inductively coupled plasma mass spectrometer (fs-LA-MC-ICP-MS) at the State Key Laboratory of Continental Dynamics (SKLCD), Northwest University, Xian, China. The equipment consisted of a 193 nm NWRfemto (RESOlution M-50, ASI) laser ablation system coupled with a Nu Plasma II MC-ICP-MS (NU Instruments Ltd., Wrexham, UK). The ablated materials were transported into the plasma using He as a carrier gas. In a cyclone coaxial mixer, Ar gas was mixed with the carrier gas before being transported into the ICP torch. The energy fluence of the laser was approximately 3.5–4 J/cm^2. The beam diameter was 35 μm with a laser repletion rate of 3–4 Hz for single spot analysis. Standard PSPT-3 (sphalerite; $\delta^{34}S_{V\text{-}CDT}$ = 26.5 ± 0.2‰) was used as certified reference material. Detailed analysis parameters are described in Bao et al. [54], Chen et al. [55] and Yuan et al. [56]. In this study, the S isotope ratios of the anglesite and associated galena, pyrite, sphalerite and chalcopyrite are given in standard notation (per mil) relative to Vienna Canyon Diablo Troilite.

3.5. In Situ Pb Isotope Analysis

In situ measurements of Pb isotope compositions of the anglesite and galena were analyzed on DSPSs using a 193 nm fs-LA-MC-ICP-MS at the SKLCD. To remove potential contamination, anhydrous ethanol was used to carefully clean the surfaces of the DSPSs prior to laser ablation analysis. Analytical spots were carefully selected to prevent the possible influence of inclusions and impurities. High-temperature-activated carbon was used to filter Hg contained in the carrier gas, which lowered both the Hg background and the detection limit. An internal Tl isotope reference NIST SRM997 in conjunction with an external reference NIST SRM 610 were used to correct for fractionation and mass discrimination effects, where the Tl solution is introduced through the CETAC Aridus II desolvation nebulizer system. The exponential law correction method for Tl normalization with optimally adjusted Tl ratio was used to obtain Pb isotopic data with high precision and accuracy [57]. The measured isotopic ratios were in agreement with the reference and published values within 2σ measurement uncertainty [54,56–58].

4. Results

4.1. Occurrence and Major and Trace Element Concentrations of Anglesite

Most seafloor hydrothermal sulfide and sulfate samples from the middle OT (MOT) Iheya North (samples H2-R1-2-a4, b3, d4) and from the southern OT (SOT) Yonaguni Knoll IV (samples H4-TVG10-2-1, and H3-T9-10-2) consist of major (>15 vol%) sphalerite, chalcopyrite, galena, pyrite and barite, with minor (<15 vol%) anglesite (Figure 3). The anglesite minerals occur as infills and veins with low Pb and high S contents in the host sulfide, as crusts with high Pb and low S contents around the margin of the relict galena, as in situ replacement or as euhedral crystals in cavities of the former, partially dissolved galena (Figures 4 and 5). This implies that low Pb and high S and high Pb and low S grains may be primary hydrothermal anglesite (PHA) and secondary supergene anglesite (SSA), respectively.

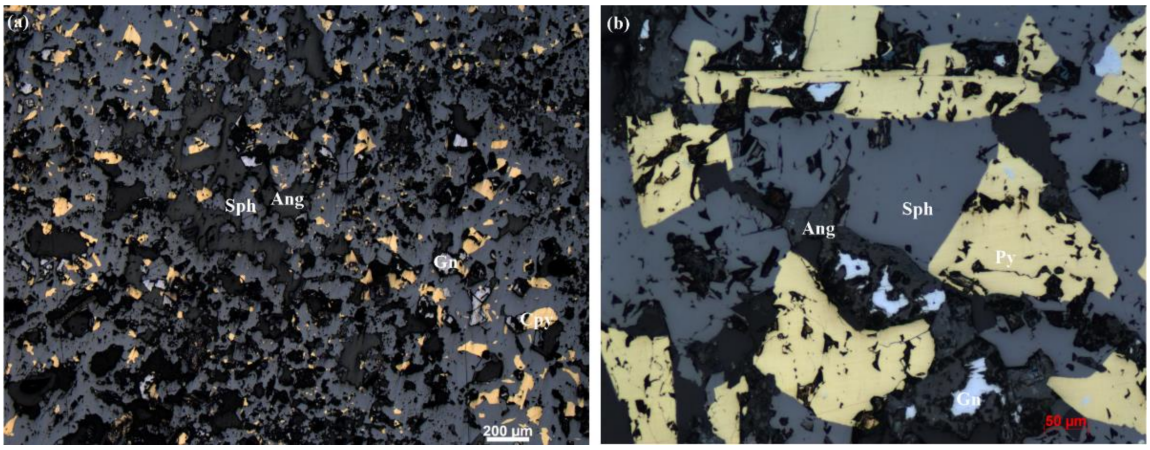

Figure 3. (**a**) Sphalerite forming large porous structures in sample H4-TVG10-2-1. Sphalerite with "dust" chalcopyrite disease condensing into larger particles. Pore centers with anglesite and galena infill indicates their later formation. (**b**) Intergrowth of subhedral to euhedral pyrite and sphalerite forming large porous structures in sample H4-TVG10-2-1; pore center filled with anglesite. Relict galena surrounded by anglesite indicates secondary origin of anglesite replacing galena. (Ang = anglesite; Sph = sphalerite; Py = pyrite; Ccp = chalcopyrite; Gn = galena).

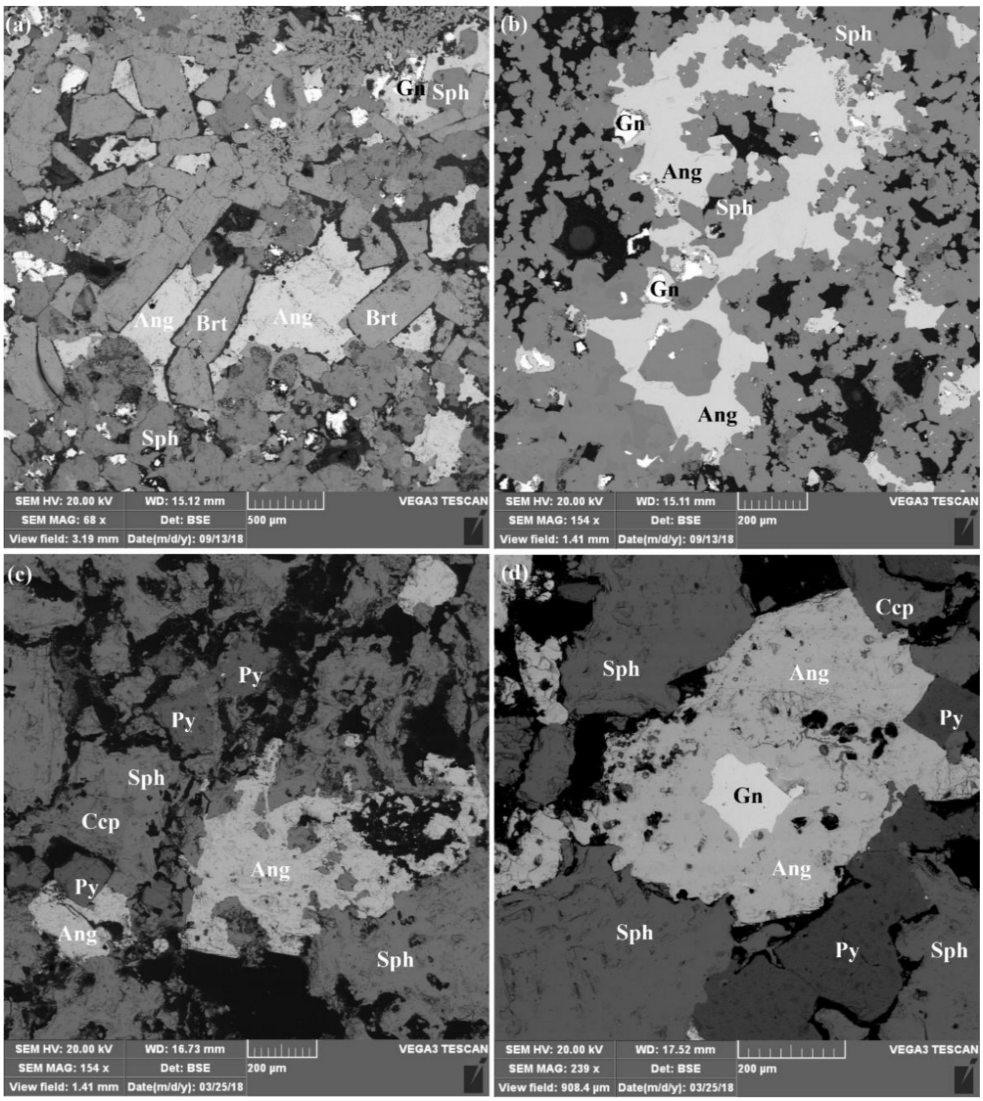

Figure 4. (**a**) SEM back-scattered electron (BSE) images of selected anglesite and sulfide minerals hosting Ag and Bi in seafloor hydrothermal sulfide deposits, Okinawa Trough. (**a**) Sample H3-T9-10-2: Intergrowth of large subhedral to euhedral barite, anglesite, sphalerite and galena forming porous structures. (**b**) Sample H4-TVG10-2-1: Anglesite replacing galena. Fluid channels with sphalerite infill indicate their later formation. (**c**) Sample H2-R1-2-a4: Intergrowth of sphalerite and pyrite forming large porous structures. Some pores filled with anglesite minerals indicate their later formation. (**d**) Sample H2-R1-2-b3: Intergrowth of sphalerite, pyrite and chalcopyrite forming porous structures. Relict galena surrounded by anglesite indicates a secondary origin of anglesite replacing galena (Ang = anglesite; Brt = barite; Sp = sphalerite; Py = pyrite; Ccp = chalcopyrite; Gn = galena).

Moreover, the PbO and SO_3 concentrations in the anglesite samples from the Iheya North hydrothermal field are more variable than those from the Yonaguni Knoll IV fields (Table S1; Figure 6a), suggesting that two types of anglesite occur in the OT back-arc basin: a high-Pb/low-S secondary supergene anglesite type (PbO > 72.50 wt.%, SO_3 < 27.00 wt.%) in the Iheya North hydrothermal field and a low-Pb/high-S type primary hydrothermal anglesite (PbO < 72.00 wt.%, SO_3 > 29.00 wt.%) in the Yonaguni Knoll IV hydrothermal fields (Figure 6a).

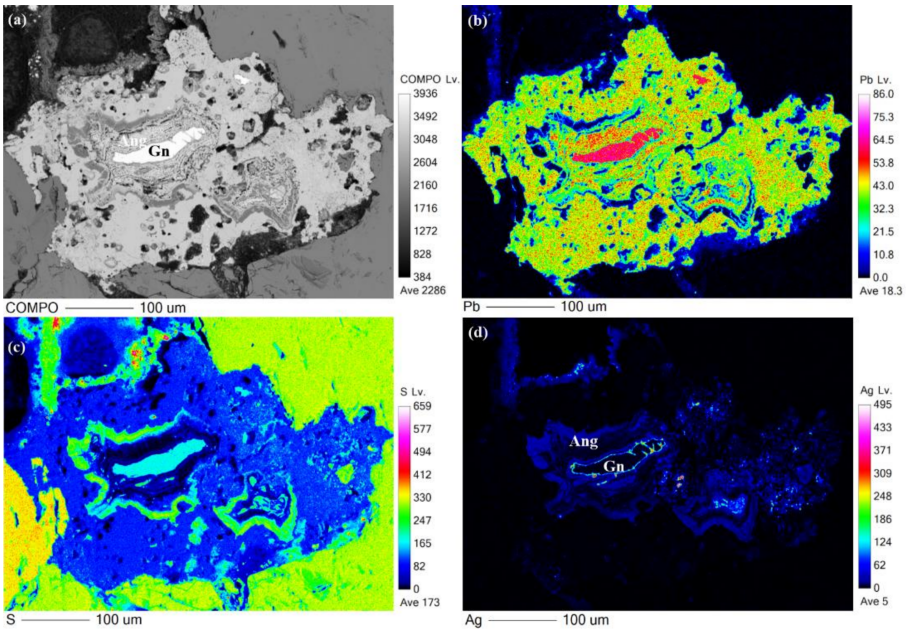

Figure 5. (**a**) BSE image of Ag–Bi-enriched anglesite and galena. X-ray elemental distribution maps after EPMA of BSE image, showing compositional heterogeneity of anglesite crystals in (**b**) Pb; (**c**) S; (**d**) galena with Ag-enriched anglesite rim and veins.

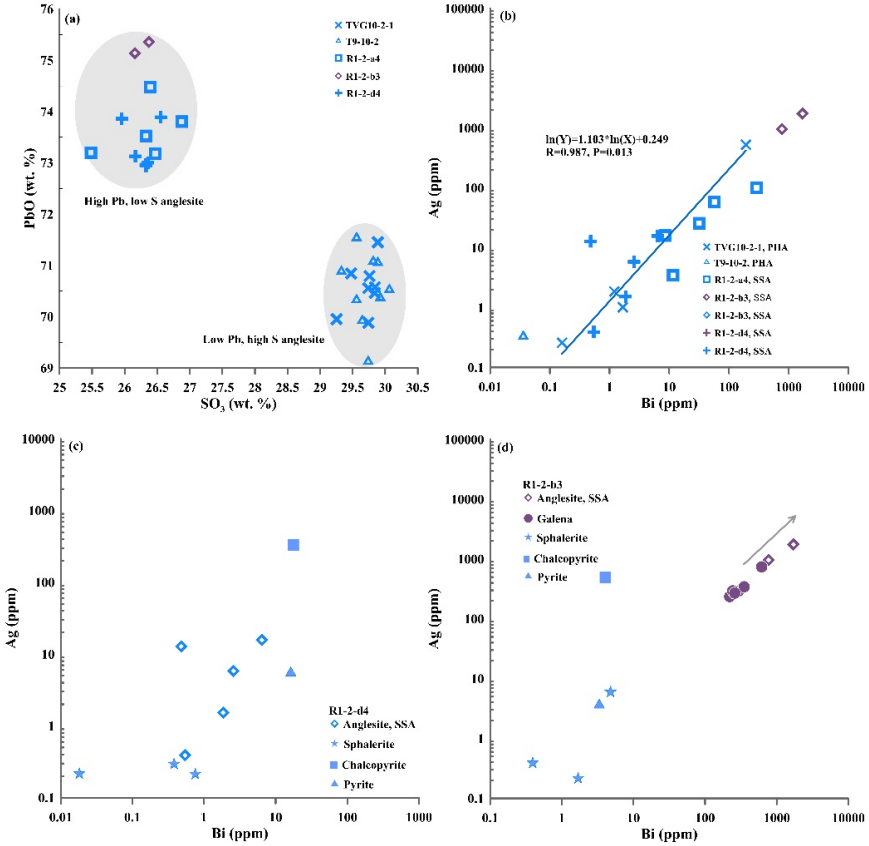

Figure 6. Plots of anglesite minerals in samples H2-R1-2-a4, b3, d4 (MOT hydrothermal field) and samples H3-T9-10-2 and H4-TVG10-2-1 (SOT hydrothermal field): (**a**) PbO vs. SO_3; (**b**) Ag vs. Bi; (**c**) Ag vs. Bi in sample H2-R1-2-d4; (**d**) Ag vs. Bi in sample H2-R1-2-b3. PHA—primary hydrothermal anglesite; SSA—secondary supergene anglesite.

Generally higher U, Cu, Th, Ni, Co and V with HREE concentrations are found in the high Pb and low S anglesites from the Iheya North than in the low Pb and high S anglesites from the Yonaguni Knoll IV hydrothermal fields (Tables S1 and S2). In addition, the Bi concentrations in the high Pb and low S anglesite samples (H2-R1-2-b3) from the Iheya North hydrothermal field are markedly more variable (0.04–3112 ppm) than for the low Pb and high S anglesite samples from the SOT hydrothermal fields (Table S2; Figure 6b). Most of the high Pb and low S anglesite from the MOT contain notably higher concentrations of both Ag and Bi than those in the high Pb and low S anglesite from the SOT (Table S2; Figure 6b). Notably, the Ag content showed a remarkable positive correlation with Bi in the anglesite in seafloor hydrothermal sulfide deposits (Figure 6b). The Mo concentrations in high Pb and low S anglesite from the Iheya North Knoll hydrothermal field are generally higher than those in the low Pb and high S anglesite from the Yonaguni Knoll IV field (Table S2; Figure 7b).

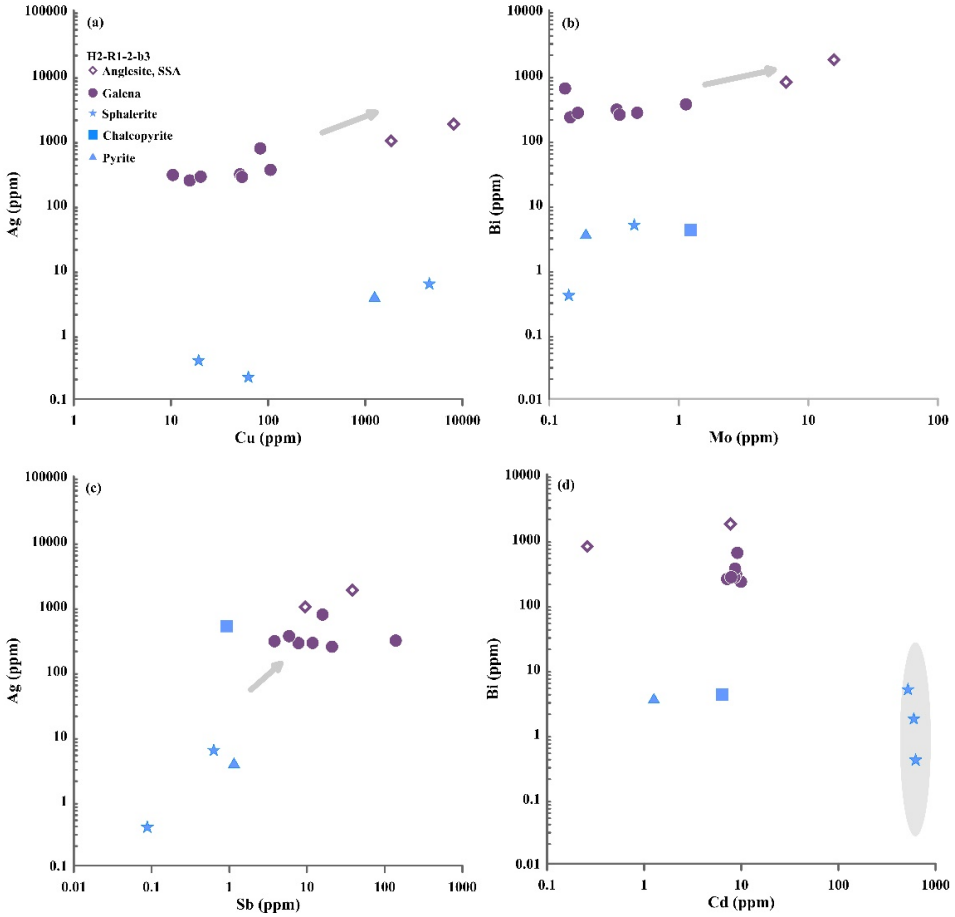

Figure 7. Plots of anglesite and sulfide minerals in sample H2-R1-2-b3: (**a**) Ag vs. Cu; (**b**) Bi vs. Mo; (**c**) Ag vs. Sb; (**d**) Bi vs. Cd. SSA—secondary supergene anglesite.

The Bi and Cu concentrations in galena associated anglesite in the Iheya North and Yonaguni Knoll IV hydrothermal fields are variable, covering the widest range (0.02–616 to 2.83–2895 ppm) (Table S2). The Sb and Ag concentrations in galena (sample H3-T9-10-2) associated anglesite from the Yonaguni Knoll IV hydrothermal field is considerably more variable (53.3–5843 and 11.4–3515 ppm) than those in the galena associated anglesite from the Iheya North hydrothermal fields (Table S2). However, most of the anglesite samples have higher Ag and Bi concentrations than the associated sulfide minerals in the OT (Table S2; Figures 6 and 7), and most of the Ag and Bi concentrations in anglesite and associated galena are considerably higher than in pyrite, chalcopyrite and sphalerite (Figures 6 and 7). The Bi/Sb ratios of galena in samples from Yonaguni Knoll IV hydrothermal field are low

than 1. In contrast, the Bi/Sb ratios of galena in samples from Iheya North hydrothermal field are much greater than 1 (Table S2).

4.2. Rare Earth Element Compositions in Anglesite

The total REE concentrations (∑REEs) in the anglesite from the OT hydrothermal fields are highly variable (0.01–30.3 ppm) (Table S2). Most of the ∑REEs in the high Pb and low S anglesite from the MOT are higher than those in the low Pb and high S anglesite from the SOT (Figure 8a). Of the high Pb and low S anglesite in the present study, those from the MOT hydrothermal fields exhibited the highest ∑REEs (30.3 ppm, sample H2-R1-2-a4, point 12-6; Table S2). However, most of the ∑REEs in the OT anglesite were higher than those in the OT associated galena (0.01–0.33 ppm) and other sulfide minerals (Table S2; Figure 8a).

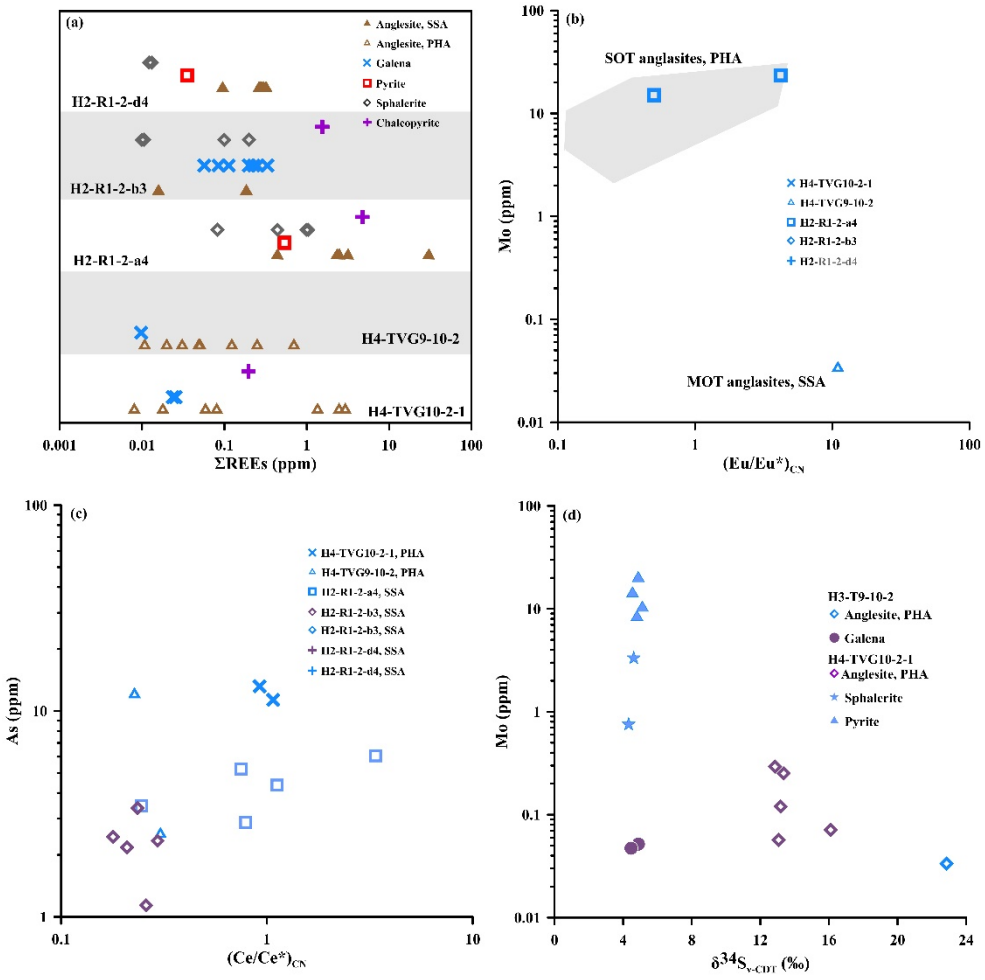

Figure 8. Plots of anglesite and sulfide minerals in OT hydrothermal sulfide deposits: (**a**) ΣREE distribution range; (**b**) Mo vs. $(Eu/Eu^*)_{CN}$; (**c**) As vs. $(Ce/Ce^*)_{CN}$; (**d**) Mo vs. $\delta^{34}S_{v\text{-}CDT}$. PHA—primary hydrothermal anglesite; SSA—secondary supergene anglesite.

The C1-chondrite-normalized REE distribution patterns of the anglesite from the OT hydrothermal fields are shown in Figure 9. The REE patterns of most of the anglesite show evidence of LREE enrichment (LREE/HREE ratios of 0.39–233), variable La_{CN}/Lu_{CN} ratios between 0.32 and 10.7, Eu anomalies ($(Eu/Eu^*)_{CN}$ ratios of 0.49–11.0) and minor Ce anomalies ($(Ce/Ce^*)_{CN}$ ratios of 0.05–3.37) (Figure 8b,c). Most of the $(Eu/Eu^*)_{CN}$ (0.49–4.21) and $(Ce/Ce^*)_{CN}$ (0.05–3.37) ratios of the high Pb and low S anglesite from the MOT are lower and higher than those (3.45–11.0, 0.06–1.07) in the low Pb and high S anglesite from the SOT, respectively. In comparison, the Eu and Ce anomalies in the galena and other

sulfides associated anglesite have a $(Eu/Eu^*)_{CN}$ ratio of 0.83 and $(Ce/Ce^*)_{CN}$ ratios of 0.06–1.38.

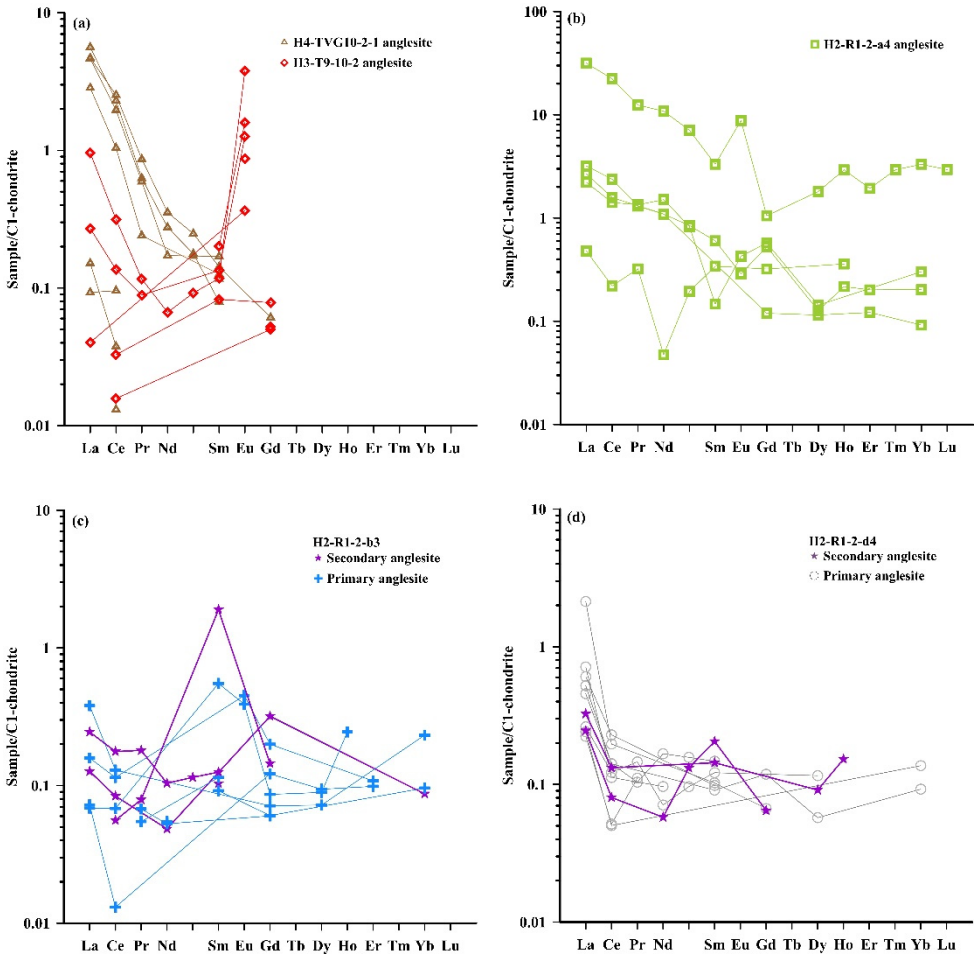

Figure 9. REE patterns of anglesite in samples (**a**) H4-TVG10-2-1 and H3-T9-10-2; (**b**) H2-R1-2-a4; (**c**) H2-R1-2-b3; and (**d**) H2-R1-2-d4 (Normalized data from Sun and McDonough, [53]).

4.3. In Situ S and Pb Isotopic Compositions of the Anglesite and Sulfides

Anglesite forming in the MOT (Iheya North, 11.04–17.42‰) and SOT (Yonaguni Knoll IV, 12.84–22.86‰) hydrothermal fields exhibits a range of $\delta^{34}S$ values of 11.04 to 22.86‰ (Table S3; Figure 10). Moreover, in the Okinawa Trough, the galena, pyrite, sphalerite and chalcopyrite have much lower sulfur isotope ratios than those in the associated anglesite ($\delta^{34}S$ values from –5.01 to 11.33‰, avg. 7.48‰, n = 60) (Table S3). Most of these are within the previously reported range 0.0–9.6‰ from previous analyses of seafloor hydrothermal sulfides [59,60]. In addition, the pyrite–sphalerite, sphalerite–chalcopyrite and sphalerite–galena pairs in samples H2-R1-2-a4, -b3 and -d4 display a sulfur isotopic equilibrium, according to known temperature-dependent fractionation factors, characteristic of most seafloor hydrothermal systems [61]. The formation temperatures of coexisting sulfide mineral pairs from the Iheya North Knoll hydrothermal field, as calculated by the sulfur isotope geothermometer formula [61,62], range from 248 to 333 °C (Table S4).

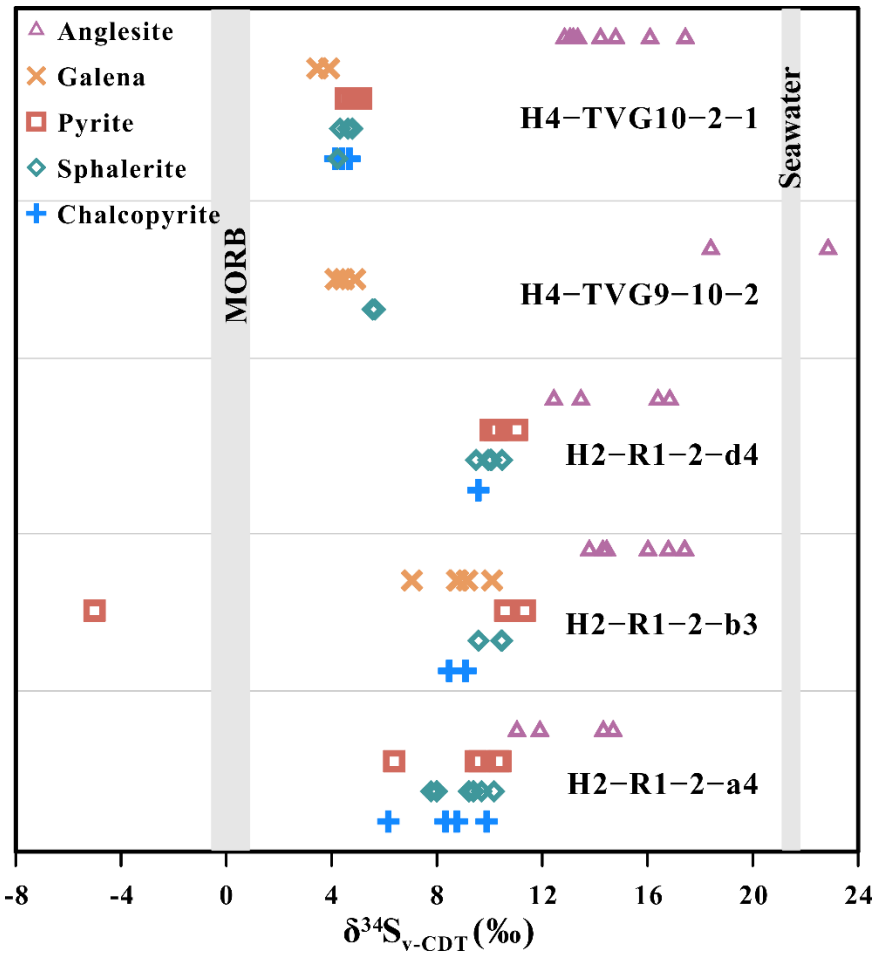

Figure 10. Sulfur isotope values for anglesite and sulfide minerals from the MOT and SOT hydrothermal sulfide deposits. MORB data from Sakai et al. [63], Alt et al. [64], Shanks et al. [65] and Alt and Shanks [66]. Seawater data from Rees et al. [67].

The anglesite in the OT hydrothermal fields have similar Pb isotopic compositions, and the Pb isotopic compositions lie within a narrow range (Table S3; Figure 11). In the Okinawa Trough, the Pb isotopic compositions of the low Pb and high S anglesite and associated galena samples from the Yonaguni Knoll IV hydrothermal fields are more radiogenic than those of the high Pb and low S anglesite and associated galena from the Iheya North hydrothermal field (Table S3; Figure 11). In addition, the $^{207}Pb/^{204}Pb$ and $^{208}Pb/^{204}Pb$ ratios of OT anglesite and associated galena are within or close to the range for the corresponding OT volcanic rocks and sediments (Figure 11).

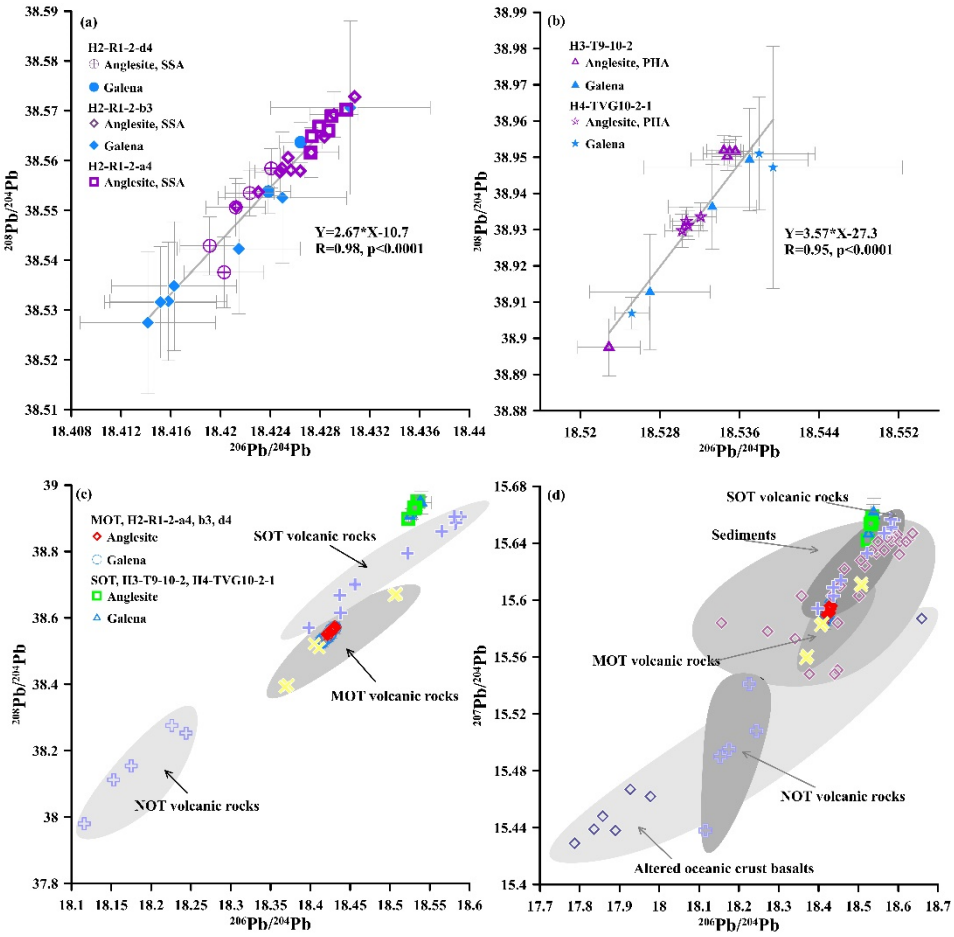

Figure 11. Plots of anglesite and galena in MOT (samples H2-R1-2-d4, b3, a4) and SOT (samples H3-T9-10-2, H4-TVG10-2-1): (**a–c**) $^{208}Pb/^{204}Pb$ vs. $^{206}Pb/^{204}Pb$; (**d**) $^{207}Pb/^{204}Pb$ vs. $^{206}Pb/^{204}Pb$. PHA—primary hydrothermal anglesite; SSA—secondary supergene anglesite. Data for NOT, MOT and SOT volcanic rock, sediment, and altered oceanic crust basalt from Shu et al. [68].

5. Discussion

5.1. Variable REE Compositions, Origin of Eu Anomalies and Sources of REEs

The ∑REEs in the anglesite in the present study vary considerably (0.01–30.3 ppm) (Table S2). They exhibit no systematic variation with Pb or S. The extent of fractionation of the LREEs and HREEs is highly variable in the anglesite from the OT hydrothermal fields (Table S2). The substitution of REEs into anglesite, analogous to the substitution of REEs into pyrite, chalcopyrite and sphalerite, appears to be strongly influenced by the larger ionic radii of the REEs [69,70]. Thus, greater LREE enrichment takes place in Pb-rich anglesite and associated galena than in pyrite, chalcopyrite and sphalerite minerals because of the similar ionic radii of Pb^{2+} (119 pm) and La^{3+} (103.2 pm) compared to the much smaller ionic radii of Fe^{2+} (55 pm), Cu^{2+} (73 pm) and Zn^{2+} (74 pm) [71,72].

Most of the REE patterns in low Pb and high S anglesite from the SOT hydrothermal fields (samples H3-T9-10-2, points 7-73, 2-1-18, 3-1-34, 8-1-82) exhibit positive Eu anomalies of 3.34 to 9.98 (Table S2; Figure 8b), similar to the values in the vent fluids at the Yonaguni Knoll IV, the East Pacific Rise near 13° N and the Logatchev hydrothermal fields [73–77]. These similarities suggest that this low Pb and high S anglesite is primary hydrothermal anglesite, which precipitated and inherited positive Eu anomalies from the vent fluids [70,78,79].

Most of the REE patterns in the high Pb and low S anglesite from the MOT hydrothermal fields are characterized by a negative or negligible Eu anomaly of 0.49 to 1.01 (Table S2; Figure 9), which is considered to signal low-temperature seawater [80]. This implies that

the high Pb and low S anglesite is formed under low-temperature conditions. Furthermore, the accumulation of Eu^{2+} in anglesite that formed at low-temperatures is also consistent with the fact that negative or negligible Eu anomalies are related to lower Eu content in the anglesite (<0.51 ppm) (Table S2). Consequently, the negligible or negative Eu anomalies in the anglesite have been interpreted as the result from low temperatures and a less Eu-enriched environment [73,79]. Seafloor hydrothermal recrystallization (i.e., zone refining) and secondary enrichment of Bi and Ag may also have caused remobilization of REEs, particularly Eu^{2+}, producing negligible or negative Eu anomalies in the anglesite (Figure 8b; [70]). This suggests that high Pb and low S anglesite in the MOT can be formed by a secondary supergene process.

The REEs in the anglesite may reflect the sources and evolution of hydrothermal fluids [70]. Comparisons show that the REE patterns of the low Pb and high S anglesite from the SOT Yonaguni Knoll IV hydrothermal fields are similar to those of Yonaguni Knoll IV vent fluids, with the anglesite also exhibiting LREE enrichment and positive Eu anomalies (Figure 9; [76]). Thus, the REEs in the low Pb and high S anglesite are likely to have all been derived from hydrothermal fluids that leached REEs from local sub-seafloor volcanic rocks and/or sediments [76] and incorporated them into the low Pb and high S anglesite [81,82]. Furthermore, the anglesite from the MOT and SOT exhibit markedly low Nd/Pb and Ce/Pb ratios (Figure 12), and Ce/PbO ratios show notable negative and positive correlations with BaO/La and Nd/PbO ratios (Figure 12). This might indicate the effect of fluid–sediment interaction [83–85].

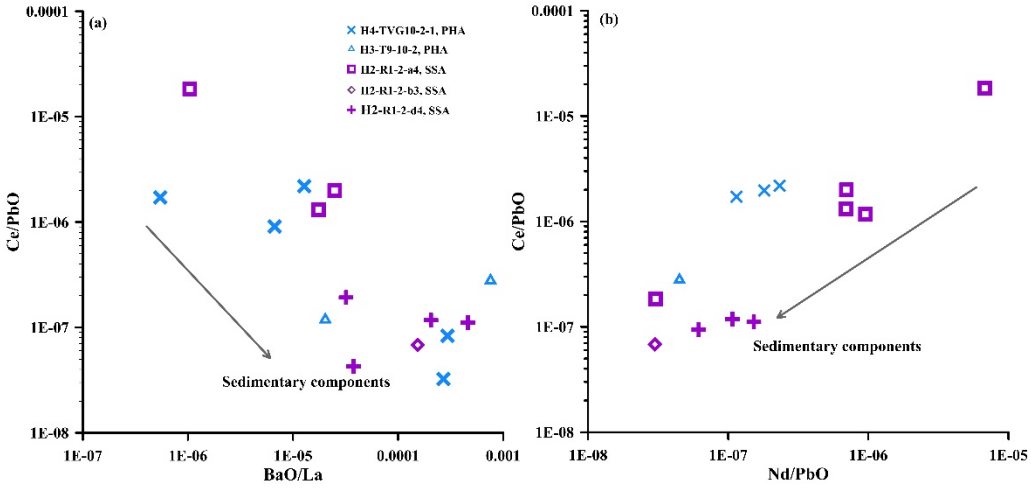

Figure 12. Plots of (**a**) Ce/PbO vs. BaO/La; and (**b**) Ce/PbO vs. Nd/PbO in anglesite minerals from the MOT (samples H2-R1-2-a4, b3, d4) and SOT (samples H3-T9-10-2, H4-TVG10-2-1) hydrothermal fields. PHA—primary hydrothermal anglesite; SSA—secondary supergene anglesite.

5.2. Sulfur Sources of Anglesite

It is known that the hydrothermal activity on the MOT and SOT hydrothermal fields is hosted by pumiceous volcaniclastic flow, sediment deposition [31], basaltic lava [42,43] and volcanic breccia [48]. The $\delta^{34}S$ values in anglesite from the OT hydrothermal fields are spread over a broad range (11.04–22.86‰; Table S3; Figure 10), which falls between the vent fluid $\delta^{34}S$ values for SO_4 (20.6–25.7‰), sediments ($\delta^{34}S$ values similar to seawater sulfate, +21‰; [67] and the vent fluid $\delta^{34}S$ values for H_2S (−0.2 to 12‰) [36,37,60,65,67,86–90], island-arc andesites and rhyolites (+4–+5‰; [91–94]), basalts (+0.1 ± 0.5‰; [63–66]) and Ryukyu Arc volcanic rocks (7.0 ± 1.9–12.9 ± 2.1‰; [91]). This suggests that the sulfur isotopic compositions in anglesite from the OT hydrothermal fields exhibit contributions of sulfur from seawater and/or sediment SO_4 and volcanic sulfur are likely to have been influenced by the mixing of seawater and/or sediment SO_4 and volcanic sulfur during anglesite formation.

However, the $\delta^{34}S$ values in the anglesite from the MOT hydrothermal fields are higher than in the associated sulfide minerals (Table S3; Figure 10), as the higher the oxidization state the more fractionation between different S species. Hence, the $\delta^{34}S$ values of anglesite are always heavier than those in the associated sulfide minerals (unless microbes are involved) and can also be thought to have been influenced considerably by the lowered seawater sulfate under more oxidizing conditions during anglesite formation [95,96].

5.3. Fluid–Rock and/or Sediment Interaction

Hydrothermal activity in the OT is hosted by volcanic rocks and sediments [31,42,43,48,97–101]. Most of the Pb isotope ratios in anglesite in the OT hydrothermal fields lie within, or close to, the range of values for rhyolitic pumices, basaltic andesites, rhyolites and sediment from the MOT (Iheya North) and SOT (Yonaguni Knoll IV) hydrothermal fields (Figure 11c,d). This suggests that OT volcanic rocks and/or sediments are the principal source of Pb in the OT hydrothermal fluids (e.g., [102–108], and the Pb isotopic compositions in the hydrothermal fluid forming anglesite are similar to those of the fluid forming associated galena in the OT hydrothermal fields. However, the Pb isotopic composition in high Pb and low S anglesite is similar to that found in associated galena in the MOT hydrothermal field, indicating that the Pb in high Pb and low S anglesite may be from the associated galena. Furthermore, the Pb isotope data for anglesite and associated sulfide cover a smaller domain than in back-arc basin volcanic rocks and sediments overall. The mean Pb isotopic compositions of anglesite from the OT hydrothermal fields (Table S3) are plotted into the ranges of Pb isotopic compositions of volcanic rocks in the different hydrothermal fields. In turn, this suggests that the Pb isotopic composition in the anglesite signifies the Pb isotopic composition of the crust and hydrothermal fluid locally. The Pb isotopic ratios of anglesite from the MOT (Iheya North) hydrothermal field appear to be comparable with the average values for volcanic rocks in the MOT (Figure 11c,d), implying that seawater is not a possible source of the Pb in the MOT anglesite.

However, comparing the more radiogenic Pb isotope composition in anglesite and associated galena from the SOT hydrothermal fields with those from the MOT hydrothermal field (Table S3) suggests that the Pb in the SOT anglesite and associated galena is possibly related to volcanism and/or sediment containing a more radiogenic Pb isotope composition. Additionally, as the Bi/Sb ratios of galena are sensitive to the host rock with Bi/Sb ratio > 1 in basic and < 1 in felsic host rocks [15], the very low Bi/Sb ratios of galena in samples from the SOT (Yonaguni Knoll IV) hydrothermal field (Table S2) suggest it was hosted by felsic rocks. This is consistent with the geological background of the hydrothermal field, which was hosted by rhyolite [101] characterized by a more radiogenic Pb isotope composition [99]. This implies that the relatively high Pb isotope ratios of low Pb and high S anglesite in the SOT are due to less seawater–volcanic rock and/or sediment interaction, which resulted in variation in hydrothermal fluid Pb isotope ratios.

Furthermore, the Pb isotopic ratios in the OT anglesite and associated galena appear to lie within or close to the range in sediments or altered oceanic crust basalts in the Philippine Sea plate ([68]; Figure 11d). This implies that subducted sedimentary and oceanic crust components are also a possible source of the Pb in the OT anglesite and associated galena by means of fluid–sediment and/or oceanic crust interaction.

5.4. The Secondary Enrichment of Bi and Ag in Secondary Supergene Anglesite

The Ag and Bi concentrations of anglesite have large ranges (Table S2), covering the range 1709 to >2000 ppm of Ag enrichment in anglesite from the oxide zone of the Prairie Creek Deposit, NW Territories, Canada [109]. The Bi and Ag concentrations of associated galena are variable (Bi: 0.02–340 avg. 57.4 ppm, n = 11; Ag: 11.4–3515 avg. 1308 ppm, n = 13) and are considerably higher than those of the vent fluid (Bi 0.000647 ppm) in the OT [87] and seawater (Bi 0.00002 ppm, Ag 0.00028 ppm) [110], which is the initial enrichment of Bi and Ag in the associated galena (Table S2, Figures 5, 6d and 7). However, the anglesite is observed to partially replace and form rims around galena crystals

(Figures 4d and 5) resulting from the alteration of galena, the reaction being PbS (s) + $2O_2$ (aq) → $PbSO_4$ (s), and the Bi and Ag concentrations in the secondary supergene anglesite (SSA) are generally higher than in neighboring galena (Table S2; Figures 3, 6d, 7a–b and 13), exhibiting secondary enrichment of Bi and Ag (Table S2; Figures 5, 6d, 7a–b and 13), resulting in most of the Ag and Bi concentrations in the high Pb and low S secondary supergene anglesite in the MOT being higher than in the low Pb and high S primary hydrothermal anglesite (Bi <200 ppm, Ag <600 ppm), which was formed by the reaction Pb^{2+} (aq) + SO_4^{2-} (aq) → $PbSO_4$ (s) (Figures 6 and 7). The implication is that back-arc hydrothermal sulfide deposits may be a potential source of enriched Ag and Bi due to supergene processes (i.e., oxidization) of seafloor hydrothermal sulfides. However, in the prevailing acidic environment (pH ≈ 5.8), the fluid reacts with the galena with increasing lead activity and decreasing pH until the anglesite stability field is reached [7]. This explains the commonly observed in situ transformation of galena to anglesite in textural coexistence (Figures 4 and 5). The fluid precipitates anglesite that is influenced by the low P_{CO2} of seafloor hydrothermal vent fluid and the higher fluid/mineral ratios [7].

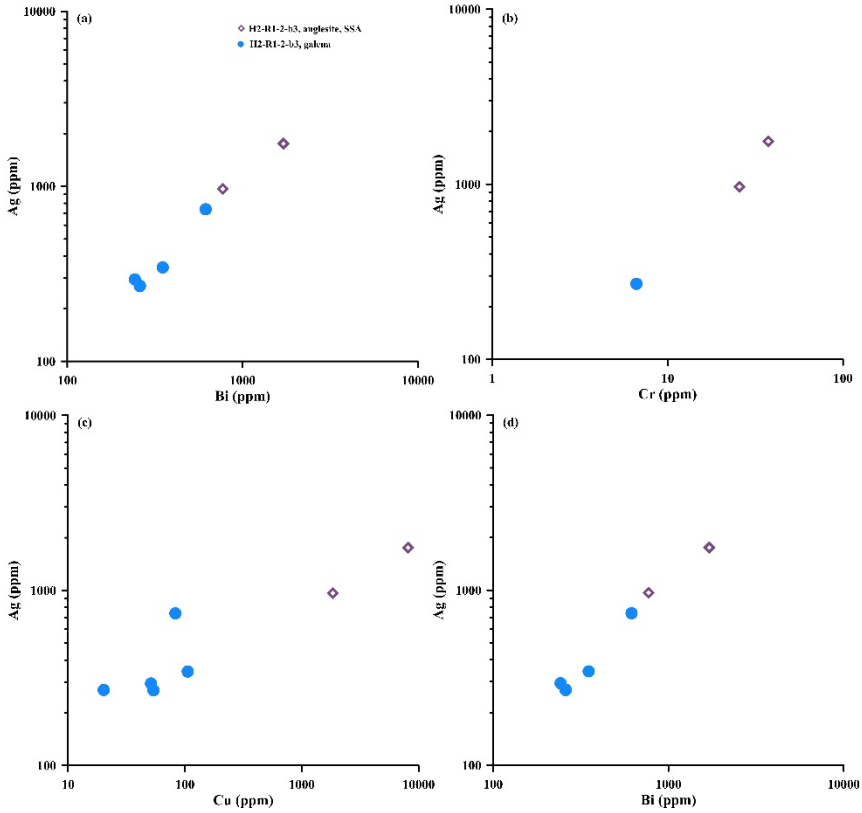

Figure 13. Plots of anglesite and neighboring galena from the MOT hydrothermal field (sample H2-R1-2-b3): (**a**) Ag vs. Sr; (**b**) Ag vs. Cr; (**c**) Ag vs. Cu; (**d**) Ag vs. Bi. SSA—secondary supergene anglesite.

Furthermore, the Pb isotopic compositions in the secondary supergene anglesite (SSA) are similar to those of associated galena in the MOT hydrothermal field (Figure 11a), suggesting that the SSA inherited the Pb isotopic compositions of galena during anglesite formation by galena alteration. However, a notable positive correlation is observed between Bi and Ag and between Mo and Cu concentrations (up to 8144 ppm) in the anglesite from the MOT hydrothermal fields (Figure 14). Cu-enriched sulfates (e.g., atacamite) are characteristic of oxidation of Cu-sulfide minerals by seawater [111], implying that Bi and Ag become enriched in anglesite in low-temperature (<100 °C) conditions. Most of the Ag, Cu, Ni, V and HREEs with Pb concentrations of SSA from the MOT (Iheya North) were generally higher than those of primary hydrothermal anglesite (PHA) from the SOT (Yonaguni Knoll IV) hydrothermal fields (Table S2), also indicating that the formation

temperature of the SSA in the MOT is lower than those of the PHA in the SOT. Furthermore, the Bi and Ag in anglesite from the OT hydrothermal fields are positively correlated with Cu and Mo (Figure 14), which might indicate that Bi and Ag are incorporated into the PHA at higher temperatures, possibly 300 °C or more. The Ag concentrations also show positive correlations with Sr, Cr, Cu and Bi concentrations in SSA and neighboring galena from the MOT hydrothermal field (Figure 13). Most of Bi (<100 ppm), Ag (<600 ppm), Se (<60 ppm) and Sb (<180 ppm) concentrations in the PHA are significantly smaller than the concentrations in SSA, which perhaps suggests that Sr, Cr, Cu, Bi, Tl, Se, Sb and Ag are incorporated into the SSA from the neighboring galena during its alteration.

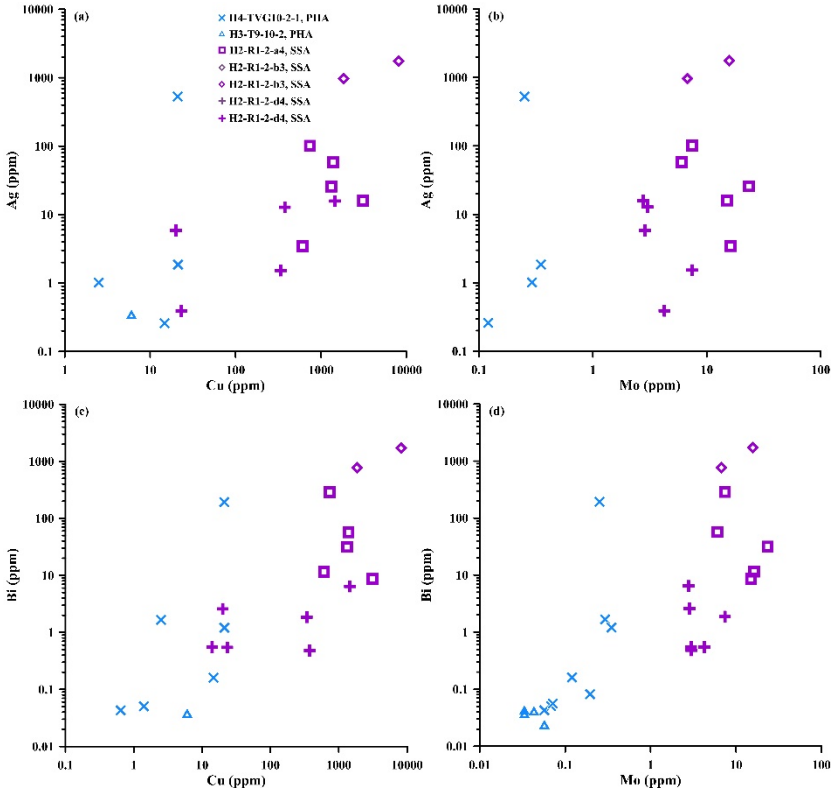

Figure 14. Plots of anglesite from MOT (samples H2-R1-2-a4, b3, d4) and SOT (samples H3-T9-10-2, H4-TVG10-2-1) hydrothermal fields: (**a**) Ag vs. Cu; (**b**) Ag vs. Mo; (**c**) Bi vs. Cu; (**d**) Bi vs. Mo. PHA—primary hydrothermal anglesite; SSA—secondary supergene anglesite.

6. Conclusions

There are two types of anglesite minerals in the OT seafloor hydrothermal fields, high Pb/low S secondary supergene anglesite and low Pb/high S primary hydrothermal anglesite. The primary hydrothermal anglesite occurs in the pores precipitated from hydrothermal fluid and intergrowth with pyrite and sphalerite in the SOT hydrothermal field. The secondary supergene anglesite is formed by the low-temperature alteration of galena, surrounding the relict galena in the MOT hydrothermal field. The galena alteration results in most of the Sr, Cr, Cu, Bi, Se, Sb and Ag being incorporated into the secondary supergene anglesite from the neighboring galena, and most of the Sr, Cr, Se, Sb, Pb with Bi and Ag concentrations in the primary hydrothermal anglesite being considerably lower than in secondary supergene anglesite. However, the secondary supergene anglesite exhibits notably higher Ag and Bi concentrations than in primary hydrothermal anglesite, galena, pyrite, sphalerite and chalcopyrite, resulting in a redistribution of Ag and Bi in seafloor sulfide deposits. Furthermore, the Ag and Bi concentrations in the galena (initially from Ag and Bi enrichment of hydrothermal fluid during galena deposition) are higher than in the primary hydrothermal anglesite. This suggests that Bi and Ag enrichment in the seafloor hydrothermal sulfide deposits is the result of Bi and Ag twice enrichment

during ore-forming processes, which also offered new evidence for the element multi-enrichment hypothesis of global hydrothermal sulfide deposits. Thus, it is possible that a valuable Bi- and Ag-enriched anglesite and associated galena will be discovered in back-arc seafloor hydrothermal sulfide deposits, and it is necessary to explore Bi and Ag deposits in those locations.

However, anglesite from the OT seafloor hydrothermal fields contains a wide and varying range of ∑REEs. Most of the secondary supergene anglesite contains lower ΣREE concentrations than the primary hydrothermal anglesite. They are notably more enriched in LREEs than in HREEs. The REEs in the low Pb and high S anglesite, which exhibit positive Eu anomalies, similar to the values in the vent fluids, are likely to have all been derived from hydrothermal fluids that leached REEs from local volcanic rocks and/or sediments. The negative or negligible Eu anomalies of the REE patterns in the high Pb and low S anglesite from the MOT hydrothermal fields are considered to signal low-temperature seawater. However, secondary enrichment of Bi and Ag during secondary supergene anglesite formation may also have caused remobilization of Eu^{2+}, resulting in negligible or negative Eu anomalies in the secondary supergene anglesite.

The sulfur isotopic compositions in anglesite in the OT hydrothermal fields vary between 11.04 and 22.86‰ for $\delta^{34}S$. These are higher than the corresponding values in associated sulfide minerals in the same hydrothermal field and are similar to those for seawater and/or sediment sulfates. This may be an indication that the sulfur in the OT anglesite samples was derived mainly from a mixing of seawater and/or sediment sulfate and volcanic sulfur. In addition, the pyrite–sphalerite, sphalerite–galena and sphalerite–chalcopyrite pairs of sulfide minerals in the OT hydrothermal fields lie within the equilibrium temperature range, suggesting that the formation temperature of pyrite, sphalerite, galena and chalcopyrite is between 248 and 333 °C.

In contrast to the mixed-origin source of S in the anglesite, most of the Pb isotopic compositions in the anglesite are identical to OT volcanic rock values, falling within or close to the range of Pb isotopic compositions found in sediments and altered oceanic crust. This suggests that the Pb in the anglesite has mainly been leached from local volcanic rocks and/or sediments that host the sub-seafloor hydrothermal systems in the OT back-arc basin. However, the Pb isotope composition of the SSA was found to be consistent with that of the associated galena, suggesting that it inherited the Pb isotopic composition during the galena alteration process. Furthermore, the Pb isotopic compositions in the anglesite from the OT hydrothermal fields are very homogeneous and cover a narrow range within, or close to, the scope of the large dataset of Pb isotopic compositions in the OT volcanic rocks, subducted sediments and altered oceanic crustal basalts. This emphasizes the importance of determining Pb isotopic compositions in anglesite from the seafloor hydrothermal sulfide deposits and implies a new means of understanding the influence of plate subduction in back-arc hydrothermal and magmatic systems. Additionally, the crystallographic difference, if any, between primary and secondary anglesite is an interesting subject to be studied in the future by X-ray diffraction due to the non-stoichiometric balance between sulfur and lead.

Supplementary Materials: The following are available online at https://www.mdpi.com/article/10.3390/jmse10010035/s1, Table S1: Electron microprobe analyses of anglesite and sulfide minerals in seafloor hydrothermal sulfide samples from the Yonaguni Knoll IV and Iheya North hydrothermal fields (wt.%) and their atoms per formula unit for elements, Table S2: LA-ICP-MS trace element concentrations in anglesite and sulfide minerals in seafloor hydrothermal sulfide samples from the Yonaguni Knoll IV and Iheya North hydrothermal fields (ppm), Table S3: LA-MC-ICP-MS sulfur and lead isotopic compositions of anglesite and sulfide minerals in seafloor hydrothermal sulfide samples from the Yonaguni Knoll IV and Iheya North hydrothermal fields, Table S4: Sulfur isotopic compositions of coexisting sulfide mineral phases in seafloor hydrothermal sulfide samples from the Iheya North hydrothermal fields, and corresponding temperature (°C) calculated by geothermometers based on equilibrium sulfur isotope fractionation factors (A) of sulfides with respect to H_2S (after Ohmoto and Rye, [62]).

Author Contributions: Z.Z.—Conceptualization, Data curation, formal analysis, funding acquisition, writing and editing. Z.C.—Data curation, formal analysis, validation. H.Q.—Data curation, methodology, validation. All authors have read and agreed to the published version of the manuscript.

Funding: This research was funded by the NSFC Major Research Plan on West-Pacific Earth System Multispheric Interactions, grant number 91958213; the Strategic Priority Research Program of the Chinese Academy of Sciences, grant number XDB42020402; the Special Fund for the Taishan Scholar Program of Shandong Province, grant number ts201511061 and the National Key Basic Research Program of China, grant number 2013CB429700.

Institutional Review Board Statement: Not applicable.

Informed Consent Statement: Not applicable.

Data Availability Statement: Data can be obtained from the corresponding author and are available online at Supplementary Materials.

Acknowledgments: We would like to thank the crews of the R/V KEXUE during the HOBAB 2, 3 and 4 cruises for their help with sample collection. We are most grateful for the detailed and constructive comments and suggestions provided by three anonymous reviewers, which greatly improved an earlier version of the manuscript. We thank the editors of MDPI for their efficient editor works.

Conflicts of Interest: The authors declare no conflict of interest.

References

1. Barton, P.B.; Bethke, P.M.; Roedder, E. Environment of ore deposition in the Creede mining district, San Juan Mountains, Colorado; Part III, Progress toward interpretation of the chemistry of the ore-forming fluid for the OH Vein. *Econ. Geol.* **1977**, *72*, 1–24. [CrossRef]
2. Fanfani, L.; Zuddas, P.; Chessa, A. Heavy metals speciation analysis as a tool for studying mine tailings weathering. *J. Geochem. Explor.* **1997**, *58*, 241–248. [CrossRef]
3. Szczerba, M.; Sawłowicz, Z. Remarks on the origin of cerussite in the Upper Silesian Zn-Pb deposits, Poland. *Mineralogia* **2009**, *40*, 54–64. [CrossRef]
4. Lara, R.H.; Briones, R.; Monroy, M.G.; Mullet, M.; Humbert, B.; Dossot, M.; Naja, G.M.; Cruz, R. Galena weathering under simulated calcareous soil conditions. *Sci. Total Environ.* **2011**, *409*, 3971–3979. [CrossRef] [PubMed]
5. Nordstrom, D.K. Hydrogeochemical processes governing the origin, transport and fate of major and trace elements from mine wastes and mineralized rock to surface waters. *Appl. Geochem.* **2011**, *26*, 1777–1791. [CrossRef]
6. Ayuso, R.A.; Foley, N.K.; Seal II, R.R.; Bove, M.; Civitillo, D.; Cosenza, A.; Grezzi, G. Lead isotope evidence for metal dispersal at the Callahan Cu–Zn–Pb mine: Goose Pond tidal estuary, Maine, USA. *J. Geochem. Explor.* **2013**, *126*, 1–22. [CrossRef]
7. Keim, M.F.; Markl, G. Weathering of galena: Mineralogical processes, hydrogeochemical fluid path modeling, and estimation of the growth rate of pyromorphite. *Am. Miner.* **2015**, *100*, 1584–1594. [CrossRef]
8. Courtin-Nomade, A.; Waltzing, T.; Evrard, C.; Soubrand, M.; Lenain, J.-F.; Ducloux, E.; Ghorbel, S.; Grosbois, C.; Bril, H. Arsenic and lead mobility: From tailing materials to the aqueous compartment. *Appl. Geochem.* **2016**, *64*, 10–21. [CrossRef]
9. Paradis, S.; Simandl, G.J.; Keevil, H.; Raudsepp, M. Carbonate-Hosted Nonsulfide Pb-Zn Deposits of the Quesnel Lake District, British Columbia, Canada. *Econ. Geol.* **2016**, *111*, 179–198. [CrossRef]
10. Jazi, M.A.; Karimpour, M.H.; Shafaroudi, A.M. Nakhlak carbonate-hosted Pb(Ag) deposit, Isfahan province, Iran: A geological, mineralogical, geochemical, fluid inclusion, and sulfur isotope study. *Ore Geol. Rev.* **2017**, *80*, 27–47. [CrossRef]
11. Keim, M.F.; Gassmann, B.; Markl, G. Formation of basic lead phases during fire-setting and other natural and man-made processes. *Am. Mineral. J. Earth Planet. Mater.* **2017**, *102*, 1482–1500. [CrossRef]
12. McClenaghan, M.; Parkhill, M.; Pronk, A.; Sinclair, W. Indicator mineral and till geochemical signatures of the Mount Pleasant W-Mo-Bi and Sn-Zn-In deposits, New Brunswick, Canada. *J. Geochem. Explor.* **2017**, *172*, 151–166. [CrossRef]
13. McClenaghan, M.B.; Paulen, R.C.; Oviatt, N.M. Geometry of indicator mineral and till geochemistry dispersal fans from the Pine Point Mississippi Valley-type Pb-Zn district, Northwest Territories, Canada. *J. Geochem. Explor.* **2018**, *190*, 69–86. [CrossRef]
14. Dill, H.G.; Weber, B.; Botz, R. Metalliferous duricrusts ("orecretes")-markers of weathering: A mineralogical and climatic-geomorphological approach to supergene Pb-Zn-Cu-Sb-P mineralization on different parent materials. *Neues Jahrb. Mineral. Abh.* **2013**, *190*, 123–195. [CrossRef]
15. Dill, H.G. Die Vererzung am Westrand der Bhmischen Masse-Metallogenese in einer ensialischen Orogenzone. *Geol. Jahrb.* **1985**, *73*, 3–461.
16. Romero, F.M.; Prol-Ledesma, R.M.; Canet, C.; Alvares, L.N.; Pérez-Vázquez, R.G. Acid drainage at the inactive Santa Lucia mine, western Cuba: Natural attenuation of arsenic, barium and lead, and geochemical behavior of rare earth elements. *Appl. Geochem.* **2010**, *25*, 716–727. [CrossRef]

17. Santoro, L.; Rollinson, G.K.; Boni, M.; Mondillo, N. Automated scanning electron microscopy (qemscan(r))-based mineral identification and quantification of the jabali zn-pb-ag nonsulfide deposit (yemen). *Econ. Geol.* **2015**, *110*, 1083–1099. [CrossRef]
18. Jébrak, M.; Marcoux, É.; Nasloubi, M.; Zaharaoui, M. From sandstone- to carbonate-hosted stratabound deposits: An isotope study of galena in the Upper-Moulouya District (Morocco). *Miner. Depos.* **1998**, *33*, 406–415. [CrossRef]
19. Bernardinetti, S.; Pieruccioni, D.; Mugnaioli, E.; Talarico, F.M.; Trotta, M.; Harroud, A.; Tufarolo, E. A pilot study to test the reliability of the ERT method in the identification of mixed sulphides bearing dykes: The example of Sidi Flah mine (Anti-Atlas, Morocco). *Ore Geol. Rev.* **2018**, *101*, 819–838. [CrossRef]
20. Batonneau, Y.; Brémard, C.; Laureyns, J.; Merlin, J.C. Microscopic and imaging Raman scattering study of PbS and its photo-oxidation products. *J. Raman Spectrosc.* **2000**, *31*, 1113–1119. [CrossRef]
21. De Giudici, G.; Zuddas, P. In situ investigation of galena dissolution in oxygen saturated solution: Evolution of surface features and kinetic rate. *Geochim. Cosmochim. Acta* **2001**, *65*, 1381–1389. [CrossRef]
22. Brookins, D.G. *Eh-pH Diagrams for Geochemistry*; Springer: Berlin/Heidelberg, Germany, 1988.
23. Eary, L. Geochemical and equilibrium trends in mine pit lakes. *Appl. Geochem.* **1999**, *14*, 963–987. [CrossRef]
24. Jeong, G.Y.; Lee, B.Y. Secondary mineralogy and microtextures of weathered sulfides and manganoan carbonates in mine waste-rock dumps, with implications for heavy-metal fixation. *Am. Miner.* **2003**, *88*, 1933–1942. [CrossRef]
25. Grondijs, H.F.; Schouten, C. A study of the Mount Isa ores [Queensland, Australia]. *Econ. Geol.* **1937**, *32*, 407–450. [CrossRef]
26. Verhaert, M.; Bernard, A.; Dekoninck, A.; Lafforgue, L.; Saddiqi, O.; Yans, J. Mineralogical and geochemical characterization of supergene Cu–Pb–Zn–V ores in the Oriental High Atlas, Morocco. *Miner. Depos.* **2017**, *52*, 1049–1068. [CrossRef]
27. Lee, P.-K.; Kang, M.-J.; Choi, S.-H.; Touray, J.-C. Sulfide oxidation and the natural attenuation of arsenic and trace metals in the waste rocks of the abandoned Seobo tungsten mine, Korea. *Appl. Geochem.* **2005**, *20*, 1687–1703. [CrossRef]
28. Vitkova, M.; Ettler, V.; Šebek, O.; Mihaljevič, M. Metal-contaminant leaching from lead smelter fly ash using pH-stat experiments. *Mineral. Mag.* **2008**, *72*, 521–524. [CrossRef]
29. Gammons, C.H.; Metesh, J.J.; Snyder, D.M. A Survey of the Geochemistry of Flooded Mine Shaft Water in Butte, Montana. *Mine Water Environ.* **2006**, *25*, 100–107. [CrossRef]
30. Kimura, M. Back-arc rifting in the Okinawa Trough. *Mar. Pet. Geol.* **1985**, *2*, 222–240. [CrossRef]
31. Ishibashi, J.-I.; Ikegami, F.; Tsuji, T.; Urabe, T. Hydrothermal Activity in the Okinawa Trough Back-Arc Basin: Geological Background and Hydrothermal Mineralization. In *Subseafloor Biosphere Linked to Hydrothermal Systems: TAIGA Concept*; Ishibashi, J.-I., Okino, K., Sunamura, M., Eds.; Springer: Tokyo, Japan, 2015; pp. 337–359.
32. Sibuet, J.-C.; Deffontaines, B.; Hsu, S.-K.; Thareau, N.; Le Formal, J.-P.; Liu, C.-S. Okinawa trough backarc basin: Early tectonic and magmatic evolution. *J. Geophys. Res. Space Phys.* **1998**, *103*, 30245–30267. [CrossRef]
33. Yan, Q.; Shi, X. Petrologic perspectives on tectonic evolution of a nascent basin (Okinawa Trough) behind Ryukyu Arc: A review. *Acta Oceanol. Sin.* **2014**, *33*, 1–12. [CrossRef]
34. Zeng, Z.; Wang, X.; Chen, C.-T.A.; Qi, H. Understanding the Compositional Variability of the Major Components of Hydrothermal Plumes in the Okinawa Trough. *Geofluids* **2018**, *2018*, 1536352. [CrossRef]
35. Kawagucci, S.; Ueno, Y.; Takai, K.; Toki, T.; Ito, M.; Inoue, K.; Makabe, A.; Yoshida, N.; Muramatsu, Y.; Takahata, N.; et al. Geochemical origin of hydrothermal fluid methane in sediment-associated fields and its relevance to the geographical distribution of whole hydrothermal circulation. *Chem. Geol.* **2013**, *339*, 213–225. [CrossRef]
36. Nakagawa, S.; Takai, K.; Inagaki, F.; Chiba, H.; Ishibashi, J.-I.; Kataoka, S.; Hirayama, H.; Nunoura, T.; Horikoshi, K.; Sako, Y. Variability in microbial community and venting chemistry in a sediment-hosted backarc hydrothermal system: Impacts of subseafloor phase-separation. *FEMS Microbiol. Ecol.* **2005**, *54*, 141–155. [CrossRef] [PubMed]
37. Kawagucci, S.; Chiba, H.; Ishibashi, J.-I.; Yamanaka, T.; Toki, T.; Muramatsu, Y.; Ueno, Y.; Makabe, A.; Inoue, K.; Yoshida, N.; et al. Hydrothermal fluid geochemistry at the Iheya North field in the mid-Okinawa Trough: Implication for origin of methane in subseafloor fluid circulation systems. *Geochem. J.* **2011**, *45*, 109–124. [CrossRef]
38. Kawagucci, S.; Miyazaki, J.; Nakajima, R.; Nozaki, T.; Takaya, Y.; Kato, Y.; Shibuya, T.; Konno, U.; Nakaguchi, Y.; Hatada, K. Post-drilling changes in fluid discharge pattern, mineral deposition, and fluid chemistry in the Iheya North hydrothermal field, Okinawa Trough. *Geochem. Geophys. Geosyst.* **2013**, *14*, 4774–4790. [CrossRef]
39. Sakai, H.; Gamo, T.; Kim, E.-S.; Shitashima, K.; Yanagisawa, F.; Tsutsumi, M.; Ishibashi, J.; Sano, Y.; Wakita, H.; Tanaka, T.; et al. Unique chemistry of the hydrothermal solution in the mid-Okinawa Trough Backarc Basin. *Geophys. Res. Lett.* **1990**, *17*, 2133–2136. [CrossRef]
40. Ishibashi, J.; Sano, Y.; Wakita, H.; Gamo, T.; Tsutsumi, M.; Sakai, H. Helium and carbon geochemistry of hydrothermal fluids from the Mid-Okinawa Trough Back Arc Basin, southwest of Japan. *Chem. Geol.* **1995**, *123*, 1–15. [CrossRef]
41. Ishibashi, J.-I.; Noguchi, T.; Toki, T.; Miyabe, S.; Yamagami, S.; Onishi, Y.; Yamanaka, T.; Yokoyama, Y.; Omori, E.; Takahashi, Y.; et al. Diversity of fluid geochemistry affected by processes during fluid upwelling in active hydrothermal fields in the Izena Hole, the middle Okinawa Trough back-arc basin. *Geochem. J.* **2014**, *48*, 357–369. [CrossRef]
42. Watanabe, M.; Hoshino, K.; Shiokawa, R.; Takaoka, Y.; Fukumoto, H.; Shibata, Y.; Shinjo, R.; Oomori, T. Metallic mineralization associated with pillow basalts in the Yaeyama Central Graben, Southern Okinawa Trough, Japan. *JAMSTEC Rep. Res. Dev.* **2006**, *3*, 1–8. [CrossRef]

43. Fukuba, T.; Noguchi, T.; Fujii, T. The Irabu Knoll: Hydrothermal Site at the Eastern Edge of the Yaeyama Graben. In *Subseafloor biosphere linked to hydrothermal systems: TAIGA Concept*; Ishibashi, J.-I., Okino, K., Sunamura, M., Eds.; Springer: Tokyo, Japan, 2015; pp. 493–496.
44. Nakano, A. Geochemistry of hydrothermal fluids from the Hatoma Knoll in the South Okinawa Trough. *JAMSTEC J. Deep. Sea Res.* **2001**, *18*, 139–144.
45. Kawagucci, S.; Toki, T.; Ishibashi, J.; Takai, K.; Ito, M.; Oomori, T.; Gamo, T. Isotopic variation of molecular hydrogen in 20–375 °C hydrothermal fluids as detected by a new analytical method. *J. Geophys. Res. Space Phys.* **2010**, *115*, 03021. [CrossRef]
46. Kishida, K.; Sohrin, Y.; Okamura, K.; Ishibashi, J.-I. Tungsten enriched in submarine hydrothermal fluids. *Earth Planet. Sci. Lett.* **2004**, *222*, 819–827. [CrossRef]
47. Konno, U.; Tsunogai, U.; Nakagawa, F.; Nakaseama, M.; Ishibashi, J.I.; Nunoura, T.; Nakamura, K.I. Liquid CO_2 venting on the seafloor: Yonaguni Knoll IV hydrothermal system, Okinawa Trough. *Geophys. Res. Lett.* **2006**, *33*, L16607. [CrossRef]
48. Suzuki, R.; Ishibashi, J.-I.; Nakaseama, M.; Konno, U.; Tsunogai, U.; Gena, K.; Chiba, H. Diverse Range of Mineralization Induced by Phase Separation of Hydrothermal Fluid: Case Study of the Yonaguni Knoll IV Hydrothermal Field in the Okinawa Trough Back-Arc Basin. *Resour. Geol.* **2008**, *58*, 267–288. [CrossRef]
49. Zeng, Z. New hydrothermal field in the Okinawa Trough. In Proceedings of the 25th Goldschmidt Conference, Prague, Czech Republic, 16–21 August 2015; p. 3573.
50. Tsuji, T.; Takai, K.; Oiwane, H.; Nakamura, Y.; Masaki, Y.; Kumagai, H.; Kinoshita, M.; Yamamoto, F.; Okano, T.; Kuramoto, S. Hydrothermal fluid flow system around the Iheya North Knoll in the mid-Okinawa trough based on seismic reflection data. *J. Volcanol. Geotherm. Res.* **2012**, *213*, 41–50. [CrossRef]
51. Liu, Y.; Hu, Z.; Gao, S.; Günther, D.; Xu, J.; Gao, C.; Chen, H. In situ analysis of major and trace elements of anhydrous minerals by LA-ICP-MS without applying an internal standard. *Chem. Geol.* **2008**, *257*, 34–43. [CrossRef]
52. Liu, Y.; Zong, K.; Kelemen, P.; Gao, S. Geochemistry and magmatic history of eclogites and ultramafic rocks from the Chinese continental scientific drill hole: Subduction and ultrahigh-pressure metamorphism of lower crustal cumulates. *Chem. Geol.* **2008**, *247*, 133–153. [CrossRef]
53. Sun, S.-S.; McDonough, W.F. Chemical and isotopic systematics of oceanic basalts: Implications for mantle composition and processes. *Geol. Soc.* **1989**, *42*, 313–345. [CrossRef]
54. Bao, Z.; Chen, L.; Zong, C.; Yuan, H.; Chen, K.; Dai, M. Development of pressed sulfide powder tablets for in situ sulfur and lead isotope measurement using LA-MC-ICP-MS. *Int. J. Mass Spectrom.* **2017**, *421*, 255–262. [CrossRef]
55. Chen, L.; Chen, K.; Bao, Z.; Liang, P.; Sun, T.; Yuan, H. Preparation of standards for in situ sulfur isotope measurement in sulfides using femtosecond laser ablation MC-ICP-MS. *J. Anal. At. Spectrom.* **2017**, *32*, 107–116. [CrossRef]
56. Yuan, H.; Liu, X.; Chen, L.; Bao, Z.; Chen, K.; Zong, C.; Li, X.-C.; Qiu, J.W. Simultaneous measurement of sulfur and lead isotopes in sulfides using nanosecond laser ablation coupled with two multi-collector inductively coupled plasma mass spectrometers. *J. Asian Earth Sci.* **2018**, *154*, 386–396. [CrossRef]
57. Chen, K.; Yuan, H.; Bao, Z.; Zong, C.; Dai, M. Precise and accurate in situ determination of lead isotope ratios in NIST, USGS, MPI-DING and CGSG glass reference materials using femtosecond laser ablation MC-ICP-MS. *Geostand. Geoanal. Res.* **2014**, *38*, 5–21.
58. Yuan, H.; Yin, C.; Liu, X.; Chen, K.; Bao, Z.; Zong, C.; Dai, M.; Lai, S.; Wang, R.; Jiang, S. High precision in-situ Pb isotopic analysis of sulfide minerals by femtosecond laser ablation multi-collector inductively coupled plasma mass spectrometry. *Sci. China Earth Sci.* **2015**, *58*, 1713–1721. [CrossRef]
59. Hannington, M.D.; De Ronde, C.E.J.; Petersen, S.; Hedenquist, J.W.; Thompson, J.F.H.; Goldfarb, R.J.; Richards, J.P. Sea-Floor Tectonics and Submarine Hydrothermal Systems. In *One Hundredth Anniversary Volume*; Society of Economic Geologists: Littelton, Colorado, USA, 2005; pp. 111–141.
60. Zeng, Z.; Chen, S.; Ma, Y.; Yin, X.; Wang, X.; Zhang, S.; Zhang, J.; Wu, X.; Li, Y.; Dong, D.; et al. Chemical compositions of mussels and clams from the Tangyin and Yonaguni Knoll IV hydrothermal fields in the southwestern Okinawa Trough. *Ore Geol. Rev.* **2017**, *87*, 172–191. [CrossRef]
61. Ohmoto, H. Stable isotope geochemistry of ore deposits. *Rev. Mineral. Geochem.* **1986**, *16*, 491–560.
62. Ohmoto, H.; Rye, R.O. Isotopes of sulfur and carbon. In *Geochemistry of Hydrothermal Ore Deposits*, 2nd ed.; Barnes, H.L., Ed.; J Wiley and Sons: New York, NY, USA, 1979; pp. 509–567.
63. Sakai, H.; Marais, D.; Ueda, A.; Moore, J. Concentrations and isotope ratios of carbon, nitrogen and sulfur in ocean-floor basalts. *Geochim. Cosmochim. Acta* **1984**, *48*, 2433–2441. [CrossRef]
64. Alt, J.C.; Anderson, T.F.; Bonnell, L. The geochemistry of sulfur in a 1.3 km section of hydrothermally altered oceanic crust, DSDP Hole 504B. *Geochim. Cosmochim. Acta* **1989**, *53*, 1011–1023. [CrossRef]
65. Shanks, W.C.; Böhlke, J.K.; Seal, R.R. Stable isotopes in mid-ocean ridge hydrothermal systems: Interactions between fluids, minerals, and organisms. *Geophys. Monogr. Am. Geophys. Union* **1995**, *91*, 194.
66. Alt, J.C.; Shanks, W.C. Serpentinization of abyssal peridotites from the MARK area, Mid-Atlantic Ridge: Sulfur geochemistry and reaction modeling. *Geochim. Cosmochim. Acta* **2003**, *67*, 641–653. [CrossRef]
67. Rees, C.; Jenkins, W.; Monster, J. The sulphur isotopic composition of ocean water sulphate. *Geochim. Cosmochim. Acta* **1978**, *42*, 377–381. [CrossRef]

68. Shu, Y.; Nielsen, S.G.; Zeng, Z.; Shinjo, R.; Blusztajn, J.; Wang, X.; Chen, S. Tracing subducted sediment inputs to the Ryukyu arc-Okinawa Trough system: Evidence from thallium isotopes. *Geochim. Cosmochim. Acta* **2017**, *217*, 462–491. [CrossRef]
69. Alt, J.C. The chemistry and sulfur isotope composition of massive sulfide and associated deposits on Green Seamount, eastern Pacific. *Econ. Geol.* **1988**, *83*, 1026–1033. [CrossRef]
70. Mills, R.; Elderfield, H. Rare earth element geochemistry of hydrothermal deposits from the active TAG Mound, 26 N Mid-Atlantic Ridge. *Geochim. Cosmochim. Acta* **1995**, *59*, 3511–3524. [CrossRef]
71. Shannon, R.D. Revised effective ionic radii and systematic studies of interatomic distances in halides and chalcogenides. *Acta Crystallogr. Sect. A* **1976**, *32*, 751–767. [CrossRef]
72. Rimskaya-Korsakova, M.N.; Dubinin, A.V. Rare earth elements in Sulfides of submarine hydrothermal vents of the Atlantic Ocean. *Geochmica Cosmochim. Acta* **2003**, *389*, 432–436.
73. Michard, A.; Albarede, F. The REE content of some hydrothermal fluids. *Chem. Geol.* **1986**, *55*, 51–60. [CrossRef]
74. Klinkhammer, G.; Elderfield, H.; Edmond, J.; Mitra, A. Geochemical implications of rare earth element patterns in hydrothermal fluids from mid-ocean ridges. *Geochim. Cosmochim. Acta* **1994**, *58*, 5105–5113. [CrossRef]
75. Douville, E.; Bienvenu, P.; Charlou, J.L.; Donval, J.P.; Fouquet, Y.; Appriou, P.; Gamo, T. Yttrium and rare earth elements in fluids from various deep-sea hydrothermal systems. *Geochim. Cosmochim. Acta* **1999**, *63*, 627–643. [CrossRef]
76. Hongo, Y.; Obata, H.; Gamo, T.; Nakaseama, M.; Ishibashi, J.; Konno, U.; Saegusa, S.; Ohkubo, S.; Tsunogai, U. Rare Earth Elements in the hydrothermal system at Okinawa Trough back-arc basin. *Geochem. J.* **2007**, *41*, 1–15. [CrossRef]
77. Schmidt, K.; Koschinsky, A.; Garbe-Schönberg, D.; de Carvalho, L.M.; Seifert, R. Geochemistry of hydrothermal fluids from the ultramafic-hosted Logatchev hydrothermal field, 15°N on the Mid-Atlantic Ridge: Temporal and spatial investigation. *Chem. Geol.* **2007**, *242*, 1–21. [CrossRef]
78. Barrett, T.J.; Jarvis, I.; Jarvis, K.E. Rare earth element geochemistry of massive sulfides-sulfates and gossans on the Southern Explorer Ridge. *Geology* **1990**, *18*, 583–586. [CrossRef]
79. Gillis, K.; Smith, A.; Ludden, J. Trace element and Sr-isotopic contents of hydrothermal clays and sulfides from the Snake Pit hydrothermal field: ODP site 649. In *Proceedings of the Ocean Drilling Program, Mid-Atlantic Ridge; Covering Legs 106 and 109 of the Cruises of the Drilling Vessel JOIDES Resolution, St. John, Newfoundland to Malaga, Spain, Sites 648–649. Ocean Drilling Program*; Texas A&M University: College Station, TX, USA; 1990, pp. 315–319.
80. De Baar, H.J.; Brewer, P.G.; Bacon, M.P. Anomalies in rare earth distributions in seawater: Gd and Tb. *Geochim. Cosmochim. Acta* **1985**, *49*, 1961–1969. [CrossRef]
81. Piepgras, D.; Wasserburg, G. Strontium and neodymium isotopes in hot springs on the East Pacific Rise and Guaymas Basin. *Earth Planet. Sci. Lett.* **1985**, *72*, 341–356. [CrossRef]
82. Langmuir, C.; Humphris, S.; Fornari, D.; Van Dover, C.; Von Damm, K.; Tivey, M.; Colodner, D.; Charlou, J.-L.; Desonie, D.; Wilson, C.; et al. Hydrothermal vents near a mantle hot spot: The Lucky Strike vent field at 37°N on the Mid-Atlantic Ridge. *Earth Planet. Sci. Lett.* **1997**, *148*, 69–91. [CrossRef]
83. Pearce, J.A.; Peate, D.W. Tectonic implications of the composition of volcanic arc magmas. *Annu. Rev. Earth Planet. Sci.* **1995**, *23*, 251–285. [CrossRef]
84. Plank, T.; Langmuir, C.H. The chemical composition of subducting sediment and its consequences for the crust and mantle. *Chem. Geol.* **1998**, *145*, 325–394. [CrossRef]
85. Yang, Y.-Z.; Wang, Y.; Ye, R.-S.; Li, S.-Q.; He, J.-F.; Siebel, W.; Chen, F. Petrology and geochemistry of Early Cretaceous A-type granitoids and late Mesozoic mafic dikes and their relationship to adakitic intrusions in the lower Yangtze River belt, Southeast China. *Int. Geol. Rev.* **2017**, *59*, 62–79. [CrossRef]
86. Gamo, T.; Sakai, H.; Kim, E.-S.; Shitashima, K.; Ishibashi, J.-I. High alkalinity due to sulfate reduction in the CLAM hydrothermal field, Okinawa Trough. *Earth Planet. Sci. Lett.* **1991**, *107*, 328–338. [CrossRef]
87. Gamo, T. Wide variation of chemical characteristics of submarine hydrothermal fluids due to secondary modification processes after high temperature water-rock interaction: A review. In *Biogeochemical Processes and Ocean Flux in the Western Pacific*; Sakai, H., Nozaki, Y., Eds.; Terra Scientific Publishing Company (TERRAPUB): Tokyo, Japan, 1995; pp. 425–451.
88. Ishibashi, J.-I.; Urabe, T. Hydrothermal activity related to arc-backarc magmatism in the western Pacific. In *Backarc Basins*; Taylor, B., Ed.; Springer: Boston, MA, USA, 1995; pp. 451–495.
89. Kawagucci, S. Fluid geochemistry of high-temperature hydrothermal fields in the Okinawa Trough. In *Subseafloor Biosphere Linked to Hydrothermal Systems: TAIGA Concept*; Ishibashi, J.-I., Okino, K., Sunamura, M., Eds.; Springer: Tokyo, Japan, 2015; pp. 387–403.
90. Takai, K.; Nakagawa, S.; Nunoura, T. Comparative investigation of microbial communities associated with hydrothermal activities in the Okinawa trough. In *Subseafloor Biosphere Linked to Hydrothermal Systems: TAIGA Concept*; Ishibashi, J.-I., Okino, K., Sunamura, M., Eds.; Springer: Tokyo, Japan, 2015; pp. 421–435.
91. Ueda, A.; Sakai, H. Sulfur isotope study of Quaternary volcanic rocks from the Japanese Islands Arc. *Geochim. Cosmochim. Acta* **1984**, *48*, 1837–1848. [CrossRef]
92. Woodhead, J.D.; Harmon, R.S.; Fraser, D. O, S, Sr, and Pb isotope variations in volcanic rocks from the Northern Mariana Islands: Implications for crustal recycling in intra-oceanic arcs. *Earth Planet. Sci. Lett.* **1987**, *83*, 39–52. [CrossRef]
93. Herzig, P.M.; Hannington, M.D.; Arribas, A.A., Jr. Sulfur isotopic composition of hydrothermal precipitates from the Lau back-arc: Implications for magmatic contributions to seafloor hydrothermal systems. *Miner. Deposita* **1998**, *33*, 226–237. [CrossRef]

94. Chen, Z.; Zeng, Z.; Tamehe, L.S.; Wang, X.; Chen, K.; Yin, X.; Yang, W.; Qi, H. Magmatic sulfide saturation and dissolution in the basaltic andesitic magma from the Yaeyama Central Graben, southern Okinawa Trough. *Lithos* **2021**, *388*, 106082. [CrossRef]
95. Alt, J.C.; Shanks, W.C.; Bach, W.; Paulick, H.; Garrido, C.J.; Beaudoin, G. Hydrothermal alteration and microbial sulfate reduction in peridotite and gabbro exposed by detachment faulting at the Mid-Atlantic Ridge, 15°20′N (ODP Leg 209): A sulfur and oxygen isotope study. *Geochem. Geophys. Geosyst.* **2007**, *8*, 08002. [CrossRef]
96. Delacour, A.; Früh-Green, G.L.; Bernasconi, S.M.; Kelley, D.S. Sulfur in peridotites and gabbros at Lost City (30°N, MAR): Implications for hydrothermal alteration and microbial activity during serpentinization. *Geochim. Cosmochim. Acta* **2008**, *72*, 5090–5110. [CrossRef]
97. Zhang, Y.; Zeng, Z.; Chen, S.; Wang, X.; Yin, X. New insights into the origin of the bimodal volcanism in the middle Okinawa Trough: Not a basalt-rhyolite differentiation process. *Front. Earth Sci.* **2018**, *12*, 325–338. [CrossRef]
98. Zhang, Y.; Zeng, Z.; Li, X.; Yin, X.; Wang, X.; Chen, S. High-potassium volcanic rocks from the O kinawa T rough: Implications for a cryptic potassium-rich and DUPAL -like source. *Geol. J.* **2017**, *53*, 1755–1766. [CrossRef]
99. Chen, Z.; Zeng, Z.; Yin, X.; Wang, X.; Zhang, Y.; Chen, S.; Shu, Y.; Guo, K.; Li, X. Petrogenesis of highly fractionated rhyolites in the southwestern Okinawa Trough: Constraints from whole-rock geochemistry data and Sr-Nd-Pb-O isotopes. *Geol. J.* **2018**, *54*, 316–332. [CrossRef]
100. Li, X.; Zeng, Z.; Chen, S.; Ma, Y.; Yang, H.; Zhang, Y.; Chen, Z. Geochemical and Sr-Nd-Pb isotopic compositions of volcanic rocks from the Iheya Ridge, the middle Okinawa Trough: Implications for petrogenesis and a mantle source. *Acta Oceanol. Sin.* **2018**, *37*, 73–88. [CrossRef]
101. Chen, Z.; Zeng, Z.; Qi, H.; Wang, X.; Yin, X.; Chen, S.; Yang, W.; Ma, Y.; Zhang, Y. Amphibole perspective to unravel the rhyolite as a potential fertile source for the Yonaguni Knoll IV hydrothermal system in the southwestern Okinawa Trough. *Geol. J.* **2020**, *55*, 4279–4301. [CrossRef]
102. Vidal, P.; Clauer, N. Pb and Sr isotopic systematics of some basalts and sulfides from the East Pacific Rise at 21°N (project RITA). *Earth Planet. Sci. Lett.* **1981**, *55*, 237–246. [CrossRef]
103. Chen, H.J. U, Th, and Pb isotopes in hot springs on the Juan de Fuca Ridge. *J. Geophys. Res. Solid Earth* **1987**, *92*, 11411–11415. [CrossRef]
104. Hegner, E.; Tatsumoto, M. Pb, Sr, and Nd isotopes in basalts and sulfides from the Juan de Fuca Ridge. *J. Geophys. Res. Space Phys.* **1987**, *92*, 11380–11386. [CrossRef]
105. Hinkley, T.K.; Tatsumoto, M. Metals and isotopes in Juan de Fuca Ridge hydrothermal fluids and their associated solid materials. *J. Geophys. Res. Space Phys.* **1987**, *92*, 11400–11410. [CrossRef]
106. Fouquet, Y.; Marcoux, E. Lead isotope systematics in Pacific hydrothermal sulfide deposits. *J. Geophys. Res. Space Phys.* **1995**, *100*, 6025–6040. [CrossRef]
107. Charlou, J.; Donval, J.; Fouquet, Y.; Jean-Baptiste, P.; Holm, N. Geochemistry of high H2 and CH4 vent fluids issuing from ultramafic rocks at the Rainbow hydrothermal field (36°14′N, MAR). *Chem. Geol.* **2002**, *191*, 345–359. [CrossRef]
108. Yao, H.-Q.; Zhou, H.-Y.; Peng, X.-T.; Bao, S.-X.; Wu, Z.-J.; Li, J.-T.; Sun, Z.-L.; Chen, Z.-Q.; Li, J.-W.; Chen, G.-Q. Metal sources of black smoker chimneys, Endeavour Segment, Juan de Fuca Ridge: Pb isotope constraints. *Appl. Geochem.* **2009**, *24*, 1971–1977. [CrossRef]
109. Stavinga, D.; Jamieson, H.; Layton-Matthews, D.; Paradis, S.; Falck, H. Geochemical and mineralogical controls on metal(loid) mobility in the oxide zone of the Prairie Creek Deposit, NWT. *Geochem. Explor. Environ. Anal.* **2017**, *17*, 21–33. [CrossRef]
110. Turekian, K.K. *Oceans*; Prentice-Hall: Engelwood Cliffs, NJ, USA, 1968.
111. Fallon, E.K.; Petersen, S.; Brooker, R.; Scott, T.B. Oxidative dissolution of hydrothermal mixed-sulphide ore: An assessment of current knowledge in relation to seafloor massive sulphide mining. *Ore Geol. Rev.* **2017**, *86*, 309–337. [CrossRef]